

Anomalous thermal transport in Eshelby twisted van der Waals nanowires

Received: 15 December 2023

Accepted: 17 December 2024

Published online: 12 February 2025

 Check for updates

Yin Liu ^{1,9}✉, Lei Jin^{2,3,9}, Tribhuwan Pandey ^{4,9}, Haoye Sun², Yuzi Liu ⁵, Xun Li ⁵, Alejandro Rodriguez⁷, Yueyin Wang¹, Tao Zhou ⁵, Rui Chen², Yongwen Sun ⁷, Yang Yang ⁸, Daryl C. Chrzan^{2,3}, Lucas Lindsay ⁶✉, Junqiao Wu ^{2,3}✉ & Jie Yao ^{2,3}✉

Dislocations in van der Waals (vdW) layered nanomaterials induce strain and structural changes that substantially impact thermal transport. Understanding these effects could enable the manipulation of dislocations for improved thermoelectric and optoelectronic applications, but experimental insights remain limited. In this study, we use synthetic Eshelby twisted vdW GeS nanowires (NWs) with single screw dislocations as a model system to explore the interplay between dislocation-induced structural modifications and lattice thermal conductivity. Our measurements reveal a monoclinic structure stabilized by the dislocation, leading to a substantial drop in thermal conductivity for larger-diameter NWs (70% at room temperature), supported by first-principles calculations. Interestingly, we also find an anomalous enhancement of thermal conductivity with decreasing diameter in twisted NWs, contrary to typical trends in non-twisted GeS NWs. This is attributed to increased conductivity near the NW cores due to compressive strain around the central dislocations, and aligns with a density-functional-theory-informed core–shell model. Our results highlight the critical role of dislocations in thermal conduction, providing fundamental insights for defect and strain engineering in advanced thermal applications.

Low-dimensional materials, including nanowires (NWs), nanotubes and two-dimensional van der Waals (vdW) materials, have become crucial for a variety of thermoelectric and optoelectronic applications, making effective thermal management design essential^{1–8}. Engineering the dimensions and introducing defects, such as dislocations, into these materials are vital for manipulating interatomic interactions and thermal conductivity (κ). For instance, nanostructuring silicon into NWs substantially reduces κ through increased phonon–boundary

scattering, resulting in a substantial boost in thermoelectric efficiency⁴. Dislocation arrays have substantially improved thermoelectric performance in vdW materials¹ and enhanced phonon transport anisotropy in group III nitride films⁹. In two-dimensional vdW materials, manipulating layer stacking has emerged as a promising method for tailoring thermal properties^{7,10,11}. For example, random interlayer rotations in the stacking of transition metal dichalcogenides (TMDCs) lead to a very low out-of-plane κ while maintaining the in-plane κ (ref. 7). In contrast

¹Department of Materials Science and Engineering, North Carolina State University, Raleigh, NC, USA. ²Department of Materials Science and Engineering, University of California Berkeley, Berkeley, CA, USA. ³Materials Sciences Division, Lawrence Berkeley National Laboratory, Berkeley, CA, USA.

⁴Department of Physics, University of Antwerp, Antwerp, Belgium. ⁵Center for Nanoscale Materials, Nanoscience and Technology Division, Argonne National Laboratory, Lemont, IL, USA. ⁶Materials Science and Technology Division, Oak Ridge National Laboratory, Oak Ridge, TN, USA. ⁷Department of Mechanical Engineering, University of South Carolina, Columbia, SC, USA. ⁸Department of Engineering Science and Mechanics and Materials Research Institute, Pennsylvania State University, University Park, PA, USA. ⁹These authors contributed equally: Yin Liu, Lei Jin, Tribhuwan Pandey.

✉e-mail: yliu292@ncsu.edu; lindsaylr@ornl.gov; wuj@berkeley.edu; yaojie@berkeley.edu

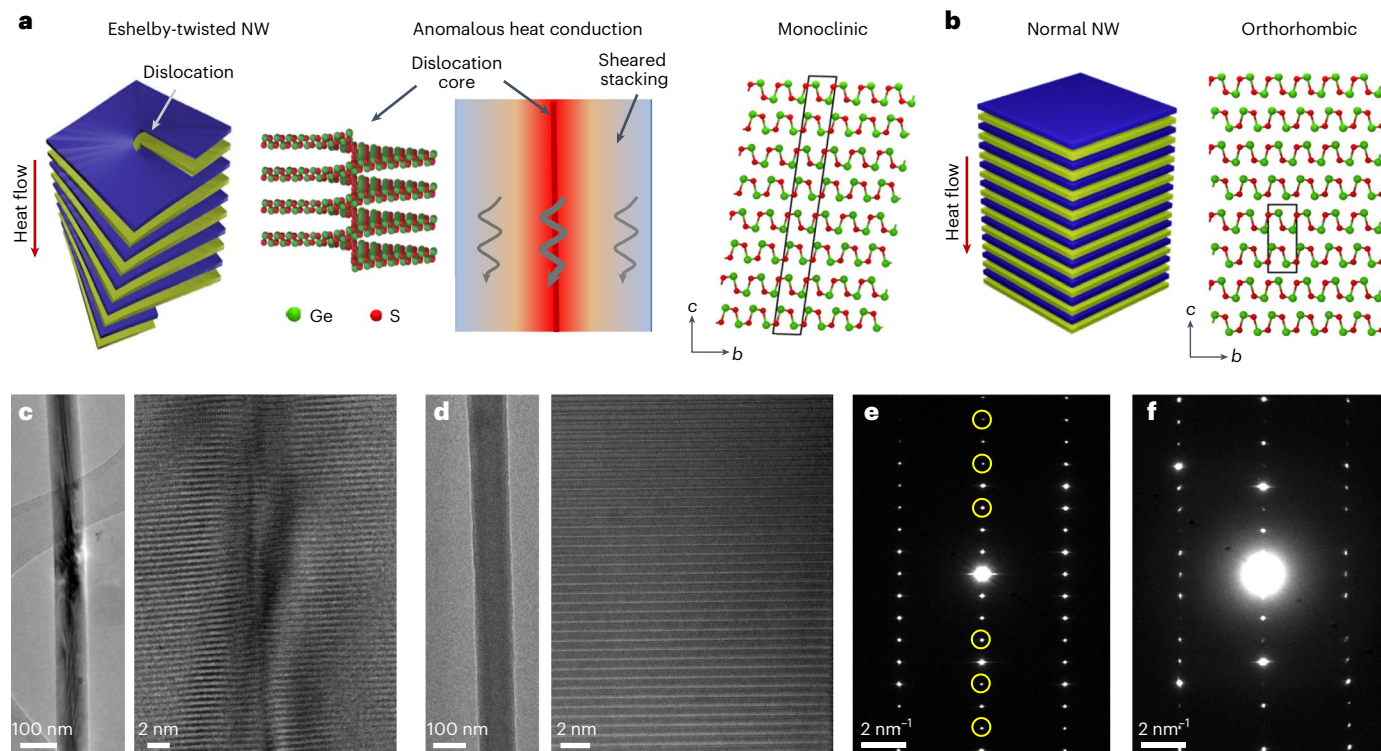


Fig. 1 | Sample characterization. **a**, Schematic illustration of an Eshelby-twisted vdW-bonded GeS NW (left), anomalous heat conduction described by a core–shell model (middle) and sheared monoclinic stacking in the shell region (right). **b**, Schematic illustration of a normal NW with orthorhombic (*pmna*) stacking. **c**, Low-magnification (left) and high-resolution (right) TEM images of a GeS NW

with Eshelby twist. **d**, Low-magnification (left) and high-resolution (right) TEM images of a normal GeS NW with no dislocation. **e, f**, SAD patterns of NWs with (e) and without (f) Eshelby twist on the same [110] zone axis. Yellow circles denote the extra spots in e not present in f.

to using the layer-by-layer construction method, the layering patterns in vdW materials can be manipulated through bottom-up synthesis processes^{12–15}, with dislocations acting as a key mechanism^{12,16,17}, which are more deployable for various applications. For example, dislocations stabilize metastable 3R-type stacked TMDCs, which display unique optical and electronic properties when compared with thermodynamically stable 2H-type TMDCs^{16,18,19}, and induce graphene spirals that exhibit extremely large magnetoresistance²⁰. However, the tuning of thermal conduction through dislocation and stacking in these synthetic vdW materials remains underexplored experimentally.

Eshelby twisted vdW NWs are valuable model systems for probing the roles of dislocation, stacking, strain and nanostructuring in thermal transport^{12,21,22}. Central screw dislocations drive the spiral growth of these NWs, while the associated strain fields induce crystallographic twisting²³ and stacking modulations²⁴. With only a single screw dislocation, these NWs allow for the investigation of isolated dislocation effects on thermal transport, unlike previous studies that involved complex dislocation distributions with unknown screw or edge characteristics⁹. While theoretical studies indicate substantial reductions in κ for Eshelby twisted NWs²⁵, experimental measurements of thermal transport have not yet been performed.

In this study, we measured the κ across vdW planes of Eshelby-twisted and non-twisted GeS NWs with varying diameters. We found about a 70% reduction in κ for large-diameter twisted NWs at room temperature when compared with non-twisted ones. This reduction is attributed to the distinct monoclinic (twisted, Fig. 1a) and orthorhombic (non-twisted, Fig. 1b) stacking structures observed in transmission electron microscopy (TEM), which agrees with our density functional theory (DFT) calculations. Surprisingly, we observed an increase in κ with decreasing diameter for twisted NWs, despite the expectation of decreased κ due to enhanced phonon–boundary scattering with decreasing diameter^{26,27}. This enhancement is

attributed to the compressive strain around the central dislocation, as supported by our four-dimensional (4D) scanning transmission electron microscopy (STEM) strain analysis and simulated using a core–shell model based on DFT calculations. Our findings provide fundamental insights into how nanostructuring and dislocations affect thermal conduction in vdW materials, crucial for thermal and thermoelectric applications.

Synthesis and structure

GeS NWs were synthesized with gold catalyst using a physical vapour transport method¹². NWs with and without the Eshelby twist, both of which have their growth directions aligned with the *c* axis perpendicular to the vdW layers (Fig. 1a,b), were grown with a ratio of -1:1. TEM characterization was conducted to distinguish the twisted and non-twisted NWs. TEM imaging of a twisted NW (Fig. 1c) reveals a dark line at the centre corresponding to the screw dislocation, along with strain-induced dark bands that vary with the rotation of the crystal planes along the *c* axis (the Eshelby twist). Atomic-resolution TEM imaging reveals lattice distortion and strain around the centre of the twisted NW. In contrast, TEM images of non-twisted NWs (Fig. 1d) have uniform contrast and undistorted lattices. Both twisted and non-twisted NWs have a thin amorphous native oxide layer at the surface, exhibiting similar surface roughnesses and thicknesses (~4–5 nm). Diffusive phonon scattering is expected at these surfaces. Selected area diffraction (SAD) patterns suggest that the non-twisted NWs have the thermodynamically stable orthorhombic structure (*pmna* space group). The twisted NWs, however, have different SAD patterns with the presence of extra diffraction spots, corresponding to a change from orthorhombic to monoclinic structure (discussed in detail later). NWs' compositions were analysed using STEM with energy dispersive X-ray spectroscopy. Both twisted and non-twisted NWs exhibit a Ge/S ratio close to 1:1, with minimal diameter variation (Supplementary Fig. 1).

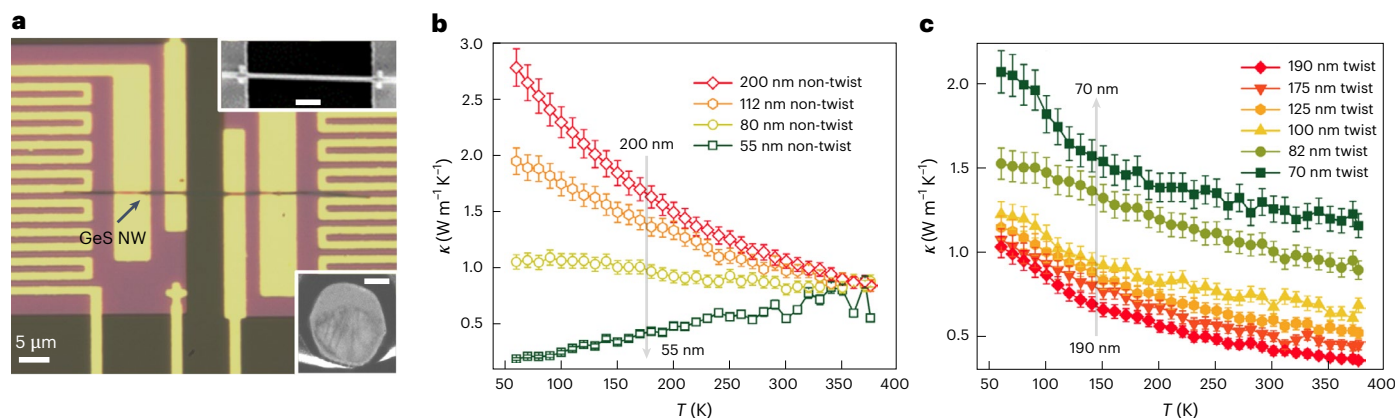


Fig. 2 | Diameter-dependent thermal conductivity of GeS NWs with and without Eshelby twist. a, Optical image of a microdevice consisting of two suspended pads bridged by a GeS NW. Insets: SEM image (upper) showing the suspended GeS NW focused ion beam (FIB)-bonded using Pt onto the pads and TEM image (lower) showing the cross-sectional area of the NW. Scale bars in the upper inset and lower inset correspond to 1 μm and 40 nm, respectively.

b,c, Temperature-dependent thermal conductivity of GeS NWs with (b) and without (c) Eshelby twist at different diameters. The uncertainties associated with the cross-sectional areas of the NWs are analysed. The data points and error bars represent the mean \pm s.d. of thermal conductivity based on three measured cross-sectional areas.

Thermal conductivity measurements

The twisted and non-twisted NWs identified by TEM imaging were transferred individually from the TEM grid to suspended pad micro-devices for κ measurements (Methods). The transferred NW bridges two suspended pads (Fig. 2a) and electron-beam-induced deposition of platinum was performed to bond the NW to the pads, reducing contact thermal resistance. The deposited Pt is confined to the suspended pad (inset of Fig. 2a), and does not extend onto the suspended NW region across the gap (Supplementary Fig. 2). The thermal conductance (G) of the NW is measured in terms of the heat transported from the heating pad to the sensing pad^{5,28–30}. The NW growth direction aligns with the c axis, leading to transport measured across the vdW planes. The in-plane κ of bulk GeS is about twice as high as the cross-plane κ . Since the cross-sectional areas of the NWs are nearly circular (inset of Fig. 2a), κ is determined on the basis of the measured thermal conductance: $\kappa = GL/\pi(d/2)^2$ with the length (L) and diameter (d) of the NWs measured using scanning electron microscopy (SEM). For direct comparisons, thermal measurements were performed on twisted and non-twisted NWs grown on the same substrate with the same synthesis conditions. Both twisted and non-twisted NWs exhibit low electronic conductivities ($<10^{-3} \text{ S m}^{-1}$) (Supplementary Fig. 3), thus the electronic contributions to κ are considered negligible and κ values are attributed solely to lattice thermal conductivity.

Two important observations can be made from the measured temperature-dependent κ of twisted and non-twisted NWs with varying diameters (Fig. 2b,c): (1) room-temperature κ of the largest-diameter twisted NW (190 nm) drops by 70% when compared with that of the largest-diameter non-twisted NW (200 nm) and (2) with decreasing diameter, κ increases for the twisted NWs, while κ decreases for the non-twisted NWs. Decreasing κ with decreasing NW diameter is typical and understood in terms of enhanced phonon–boundary scattering; while heat is carried along the NW axis, most phonons also have an in-plane velocity component and thus finite probability of scattering with the amorphous surface (see Supplementary Fig. 4 for detailed calculations). This is consistent with many diameter-dependent κ measurements in a variety of semiconductors^{4,31–37}. In stark contrast, κ of twisted NWs increases with decreasing diameter. Though the κ of the twisted NWs are smaller than those of the non-twisted NWs for $d > 110$ nm, this trend is reversed for small diameters. This suggests the existence of a mechanism that enhances κ in the twisted NWs, near the core, which more than compensates the reduction of κ due to increased surface resistance.

κ reduction in large-diameter twisted NWs

We first examine the large reduction of κ in the twisted NW in the large-diameter, bulk-like limit when compared with that of the non-twisted wire (Fig. 3a). In this limit, the effect of surface scattering is weak because the intrinsic in-plane mean free paths perpendicular to the transport direction of the heat-carrying phonons are generally smaller than the NW diameters around room temperature (Supplementary Fig. 4). In addition, any effect of the central dislocation core on thermal transport in the twisted NW is presumably weak as its cross-sectional area relative to the total is small. Therefore, the measured results are attributed to the overall structure/stacking change in the twisted wires. An overall structural change of the twisted NWs is revealed by a change of SAD patterns (compare Fig. 1e with Fig. 1f). Previous studies have shown that screw dislocation threading layers in TMDCs lead to an overall stacking change from 2H to 3R^{16,18}. The samples in those studies had a large lateral size with no twist, where the strain effects from dislocations were minimal. In contrast, substantial strain is expected in our twisted NWs.

Further understanding of the structural changes in the twisted NWs can be obtained through real-space atomic-resolution STEM imaging. However, the small NW sizes make such analysis very challenging. Thus, we performed analysis on larger twisted GeS crystals with a radial size of several micrometres resulting from radial growth from a twisted NW (Supplementary Fig. 5). The microscale GeS crystal preserves the twist rate of the NW and thus has a similar strain field¹². Atomic-resolution STEM imaging (Fig. 3b,c) along both [100] and [110] directions was performed to provide projected positions of Ge and S atoms, allowing us to unambiguously reveal a monoclinic structure due to interlayer sliding in the twisted crystal. In contrast to the standard orthorhombic structure, in which the unit cell consists of two atomic layers with AB stacking (Fig. 1b), the unit cell of the monoclinic structure (labelled in Figs. 1a and 3b,c) consists of eight atomic layers (four sets of AB stacked layers), with each AB stacked double layer sliding by $-1/4$ lattice vector along the armchair direction (b axis) in the vdW plane. The fast Fourier transform (FFT) pattern of the STEM images (inset in Fig. 3c) shows that the cross-plane (c -axis) lattice vector is not normal to the vdW plane in the monoclinic structure, matching well with the simulated FFT patterns for the structure. Our DFT calculations indicate an energy discrepancy of 0.034 eV per atom between the monoclinic and orthorhombic phases, along with an energy barrier of 0.3 eV per atom for interlayer sliding (Supplementary Fig. 6). Consistent with Eshelby's theory, the shear stress of the screw

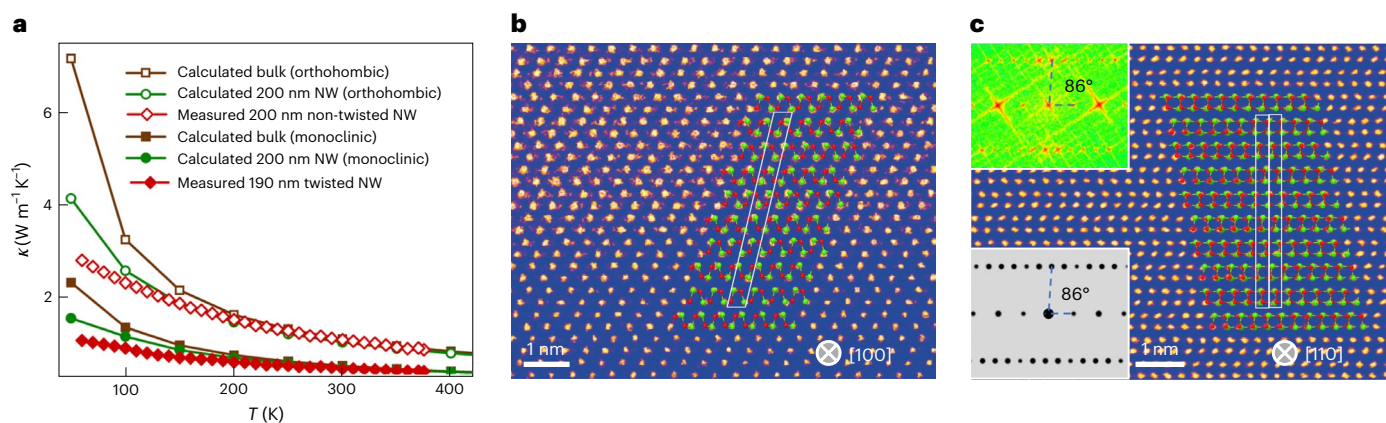


Fig. 3 | Large-diameter NW thermal conductivities (bulk limit) and STEM measurements. **a**, Measured temperature-dependent thermal conductivities of a non-twisted GeS NW with $d = 200$ nm and a twisted NW with $d = 190$ nm. Calculated temperature-dependent thermal conductivities of bulk and NW orthorhombic and monoclinic structures are also shown. **b, c**, Atomic-resolution STEM images showing the sheared ‘monoclinic’ stacking in twisted GeS crystals

along [100] (**b**) and [110] (**c**) zone axes. The overlays show the atomic structures projected along the zone axes. The monoclinic unit cell is highlighted by white parallelograms. The upper inset in **c** shows the FFT pattern of **c** and the lower inset in **c** shows the simulated FFT pattern of the monoclinic structure. The two blue dashed lines in the FFT pattern have an angle of 86° , consistent with the monoclinic structure.

dislocation induces interlayer sliding and the formation of a monoclinic structure. Indeed, the structure is only present within a distance of a few hundred nanometres from the dislocation, where the shear strain is substantial, and the structure changes to the standard orthorhombic structure at larger distances from the dislocation, where the shear strain becomes minimal. Therefore, the monoclinic stacking identified in the twisted vdW materials manifests a strong shear-strain effect, revealing a unique mechanism for modulating the interlayer stacking, different from the dislocation-induced stacking changes in non-twisted multilayer TMDCs.

The metastable monoclinic structure observed in the microscale twisted crystal suggests that shear-strain-induced interlayer sliding and stacking changes are also present in the twisted NWs. Both the magnitude of interlayer sliding and the distribution of the sheared phase are expected to vary with radial distance from the dislocation, following the changing shear strain (Supplementary Fig. 7). To gain further insight, we simulate the SAD patterns of the observed monoclinic structure (Supplementary Fig. 8), which show good agreement with measured SAD patterns of the twisted NWs (Fig. 1e). The findings indicate that the overall structure of twisted NWs can be adequately represented by the monoclinic structure. The abundant presence of the monoclinic structure in the NWs cannot be solely explained by the calculated shear-strain distribution (Supplementary Fig. 7), which anticipates a fast decline in shear strain as the radial distance increases. To understand this comprehensive structural transformation, kinetic effects must be taken into account. During growth, the monoclinic phase forms in twisted NWs when the diameter is small and shear stress is substantial. The shear stress diminishes with increasing diameter. Nonetheless, the substantial energy barrier (0.3 eV per atom) stabilizes the monoclinic phase and prevents its transition to the orthorhombic phase.

We note that Eshelby twisted NWs have an interlayer rotation that is inversely proportional to the NW diameter²³. A previous study showed that vdW MoS₂ multilayers with random interlayer rotations around tens of degrees greatly reduced the cross-plane thermal conductivity⁷. However, the layer-to-layer rotations in our Eshelby twisted GeS NWs are much smaller ($<10^{-2}$ degrees)¹², which is expected to have minimal effect on the cross-plane κ . Therefore, we attribute the low κ of twisted NWs at large diameters to the shear-strain-induced monoclinic structure.

To further understand the variations of κ of the large-diameter NWs, we calculate the cross-plane lattice κ of bulk and NW GeS in

both monoclinic and orthorhombic structures from first-principles calculations (Fig. 3a and Supplementary Fig. 9a) (details given in Methods). The calculations give lower cross-plane κ of the monoclinic phase (bulk and NW) than of the orthorhombic structure over the entire temperature range. We find that phonon group velocities (Supplementary Fig. 9b) are comparable between the two structures; however, the intrinsic phonon lifetimes (Supplementary Fig. 9c) are substantially lower in the monoclinic phase, particularly for the low-frequency heat-carrying modes, thus governing its lower κ .

The calculated κ of the separate monoclinic and orthorhombic large-diameter NWs match well with the respectively measured κ of twisted and non-twisted NWs for $T > 200$ K (Fig. 3a). Furthermore, these NW κ values are similar to those of the calculated bulk structures at higher T , consistent with weak surface scattering relative to the intrinsic anharmonic resistance. Expected discrepancies for $T < 200$ K emerge in the large-diameter NWs due to the increased importance of other possible extrinsic scattering mechanisms (for example, due to point defects) not accounted for in the models that can become more important at low temperatures, particularly in the more complex twisted NWs. At the highest temperatures, all of the non-twisted NWs have similar κ values as the intrinsic phonon–phonon scattering dominates. With decreasing T , the intrinsic scattering becomes frozen out and the diffuse surface scattering becomes more important, particularly for smaller-diameter NWs (see Supplementary Fig. 10 for calculated scattering rates). The interplay between the intrinsic scattering (temperature dependent) and the surface scattering (temperature independent) underlies the weakening of the temperature dependence of κ with decreasing diameter. For all NWs at low enough temperatures, surface scattering should dominate and κ should peak and decrease with decreasing T (not seen in measurements), tracking the vibrational specific heat^{26,27}. Calculations demonstrate that the κ peak occurs at ~ 20 – 30 K for the bulk GeS structures (Supplementary Fig. 11 and related discussion). This non-twisted NW κ behaviour is consistent with well-documented κ behaviour in covalently bonded, nearly isotropic materials^{4,28,31–37} as well as anisotropic quasi-one-dimensional materials (Ta₂Pd₃Se₈ and Ta₂Se₃) with transport along the covalent bonds^{38,39}. In contrast, the κ behaviours of the twisted NWs are confounding: (1) the temperature dependence of κ is relatively insensitive to NW diameter, (2) κ increases with decreasing diameter and (3) κ for most of the measured data is above the intrinsic calculated monoclinic bulk values (Supplementary Fig. 12).

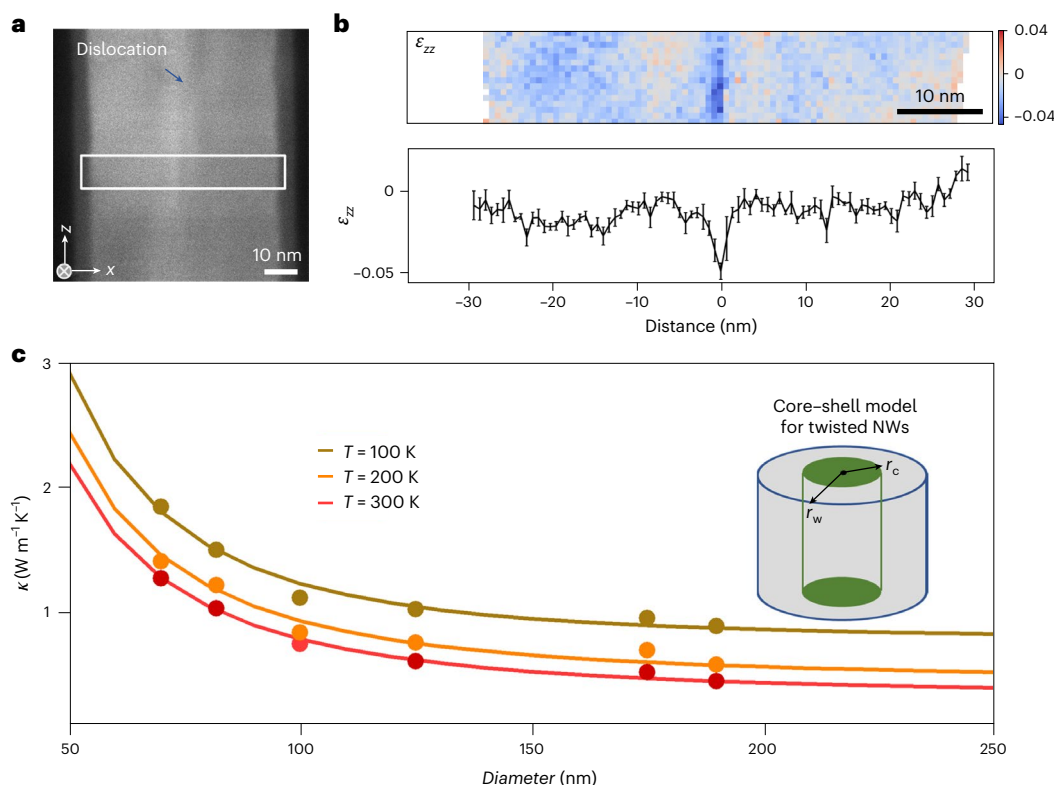


Fig. 4 | Strain-enhanced thermal conductivity in twisted NWs. **a, b**, STEM image (**a**) and corresponding distribution of compressive strain ϵ_{zz} (**b**) obtained from 4D STEM analysis of a twisted NW with $d = 70$ nm. The white box in **a** denotes the area where the strain analysis is performed. The x axis is the in-plane direction normal to the (110) planes whereas the z axis is the cross-plane direction. The lower panel

in **b** shows the average of ϵ_{zz} along the z direction as a function of distance from the central dislocation. The data points and error bars represent the mean \pm s.d. **c**, Measured (symbols) and calculated (curves) thermal conductivities for twisted NWs at different temperatures with varying diameters. Inset: schematic of the core-shell model of the twisted NW.

Anomalous diameter-dependent thermal transport in twisted NWs

We next discuss the anomalous diameter-dependent thermal transport in the twisted NWs. The structural complexity induced by the central dislocation becomes increasingly prominent as the NW cross-sectional area decreases, making the core area a larger proportion of the overall wire. We first consider that the anomalous κ may arise from electronic contributions in the dislocation region, as conductive dislocation cores have been observed in vdW and covalent materials^{40,41}. Our measurement of the electrical conductivity of twisted NWs with varying diameter shows a low electrical conductivity with no dependence on the diameter ($<10^{-3} \text{ S m}^{-1}$). The electron conductance is therefore excluded as the mechanism for the κ enhancement.

Since the measured κ data of the twisted NWs lie above the calculated intrinsic GeS monoclinic bulk values, which reproduce the high-temperature 190 nm twisted NW data well, no amount or type of extrinsic defect scattering can alone explain their κ behaviours (Supplementary Fig. 12). On the other hand, compressive strain can enhance the lattice κ ; for example, 9% compressive strain from hydrostatic pressure enhanced cross-plane κ sevenfold in multilayer MoS_2 ⁴². Our DFT calculations also demonstrate increasing κ with increasing compression on monoclinic GeS (Supplementary Fig. 13). Using a 4D STEM technique (Methods), we analyse the strain field in a twisted NW sample (Fig. 4a). Figure 4b and Supplementary Fig. 14 show maps of cross-plane normal strain (ϵ_{zz}) and in-plane normal strain (ϵ_{xx}) along the $[\bar{1}\bar{1}0]$ zone axis. The ϵ_{zz} and ϵ_{xx} strain distributions are non-uniform. Near the core of the twisted NW we observe a large cross-plane compressive strain of -5% and in-plane tensile strain of 2%. This measured strain is averaged over the NW's thickness, from the upper surface to the dislocation core and down to the lower surface. While the ϵ_{zz} strain map shows

substantial strain concentrated in a few nanometres, the actual cross-plane compressive strain around the dislocation core is probably larger and more broadly distributed than indicated in the map. The complex strain cannot be explained by classical Eshelby theory, which predicts only shear strain. It could arise from interlayer compression due to the covalently bonded dislocation core and the disassociation of the central screw into partial dislocations^{43,44}. Despite the presence of the local strains, the average strain of the twisted NW is near zero and the average lattice parameters are very similar to the lattice parameters of the non-twisted NWs.

Given the observed cross-plane strains and expected higher κ with compression⁴², we attribute the anomalous diameter dependence of κ in the twisted NWs to a strongly thermally conducting core that is little affected by decrease in the overall NW diameter. To illustrate this mechanism, we built a core-shell model (inset to Fig. 4c) of thermal transport in the twisted NWs informed by the strain measurements and DFT calculations of bulk GeS. In the unknown core region ($0 < r < r_c$) we assume a weakly T -dependent κ_{core} that decreases linearly with radial distance to κ_{shell} determined by DFT simulations of the monoclinic structure in the shell region ($r_c < r < r_w$), where r_c and $r_w = d/2$ are the core and NW radii, respectively (Methods). We also explored the effects of different extrinsic scatterings (for example, point defects) for improved model description in the low- T region (Supplementary Figs. 12 and 15–17 and corresponding discussion). This simplified core-shell model reproduces the measured temperature- and diameter-dependent κ data of the twisted NWs (Fig. 4c) from four constrained fitting parameters (Methods). The best fit parameters also give physically reasonable values for the core radius and thermal conductivity: r_c of ~ 20 nm and average room-temperature κ_{core} of $\sim 4.9 \text{ W m}^{-1} \text{K}^{-1}$, which are consistent with the strain map and

calculated increase of κ for the monoclinic phase under compression. In general, the model further supports that the increased measured κ with decreasing radius arises from reduced cross-sectional area of the weakly conducting shell relative to the strongly conducting core. Within the conducting core, compressive strain and atomic distortion near the dislocation core may bring atoms closer together, potentially forming covalent bonds that enhance cross-plane thermal conductivity. However, because of the limited spatial extent of the covalent pathway, this cannot fully explain the observed enhancement in thermal conductivity on its own (Supplementary Figs. 18 and 19 and corresponding discussion).

Outlook

In summary, our study of Eshelby-twisted vdW NWs reveals prominent and anomalous phonon transport behaviours resulting from dislocation-induced structural modifications. Dislocation shear strain induces interlayer sliding and stacking variations, substantially reducing thermal conductivity. Thus, shear strain can be used to stabilize metastable structures in vdW materials, achieving low cross-plane conductivity and high thermal anisotropy and other distinct physical properties. Conversely, local compressive strain near the dislocation core enhances thermal conductivity, resulting in an unexpected increase in κ with decreasing diameter, as illustrated by a core-shell model. This unusual transport behaviour opens avenues for addressing classical size effects in low-dimensional nanomaterials for thermal management in microelectronics. Additionally, introducing a high density of well-aligned dislocations into thin-film or bulk vdW materials can create regions with varying phases and highly conductive core channels, making it crucial to modify dislocation density, orientation and characteristics to control phase stability and material performance.

Online content

Any methods, additional references, Nature Portfolio reporting summaries, source data, extended data, supplementary information, acknowledgements, peer review information; details of author contributions and competing interests; and statements of data and code availability are available at <https://doi.org/10.1038/s41563-024-02108-3>.

References

- Kim, S. I. et al. Thermoelectrics. Dense dislocation arrays embedded in grain boundaries for high-performance bulk thermoelectrics. *Science* **348**, 109–114 (2015).
- Zhao, L.-D. et al. Ultralow thermal conductivity and high thermoelectric figure of merit in SnSe crystals. *Nature* **508**, 373–377 (2014).
- Snyder, G. J. & Toberer, E. S. Complex thermoelectric materials. *Nat. Mater.* **7**, 105–114 (2008).
- Hochbaum, A. I. et al. Enhanced thermoelectric performance of rough silicon nanowires. *Nature* **451**, 163–167 (2008).
- Kim, P., Shi, L., Majumdar, A. & McEuen, P. L. Thermal transport measurements of individual multiwalled nanotubes. *Phys. Rev. Lett.* **87**, 215502 (2001).
- Balandin, A. A. et al. Superior thermal conductivity of single-layer graphene. *Nano Lett.* **8**, 902–907 (2008).
- Kim, S. E. et al. Extremely anisotropic van der Waals thermal conductors. *Nature* **597**, 660–665 (2021).
- Chen, R., Lee, J., Lee, W. & Li, D. Thermoelectrics of nanowires. *Chem. Rev.* **119**, 9260–9302 (2019).
- Sun, B. et al. Dislocation-induced thermal transport anisotropy in single-crystal group-III nitride films. *Nat. Mater.* **18**, 136–140 (2019).
- Zhang, L. et al. Effect of twist angle on interfacial thermal transport in two-dimensional bilayers. *Nano Lett.* **23**, 7790–7796 (2023).
- Ren, W. et al. The impact of interlayer rotation on thermal transport across graphene/hexagonal boron nitride van der Waals heterostructure. *Nano Lett.* **21**, 2634–2641 (2021).
- Liu, Y. et al. Helical van der Waals crystals with discretized Eshelby twist. *Nature* **570**, 358–362 (2019).
- Zhao, Y. et al. Supertwisted spirals of layered materials enabled by growth on non-Euclidean surfaces. *Science* **370**, 442–445 (2020).
- Sun, L. et al. Hetero-site nucleation for growing twisted bilayer graphene with a wide range of twist angles. *Nat. Commun.* **12**, 2391 (2021).
- Liu, C. et al. Designed growth of large bilayer graphene with arbitrary twist angles. *Nat. Mater.* **21**, 1263–1268 (2022).
- Shearer, M. J. et al. Complex and noncentrosymmetric stacking of layered metal dichalcogenide materials created by screw dislocations. *J. Am. Chem. Soc.* **139**, 3496–3504 (2017).
- Wang, Z.-J. et al. Conversion of chirality to twisting via sequential one-dimensional and two-dimensional growth of graphene spirals. *Nat. Mater.* **23**, 331–338 (2024).
- Suzuki, R. et al. Valley-dependent spin polarization in bulk MoS₂ with broken inversion symmetry. *Nat. Nanotechnol.* **9**, 611–617 (2014).
- Wilson, J. A. & Yoffe, A. D. The transition metal dichalcogenides discussion and interpretation of the observed optical, electrical and structural properties. *Adv. Phys.* **18**, 193–335 (1969).
- Zhang, Y. et al. Extremely large magnetoresistance in twisted intertwined graphene spirals. *Nat. Commun.* **15**, 6120 (2024).
- Fang, Z. et al. Chemically modulating the twist rate of helical van der Waals crystals. *Chem. Mater.* **32**, 299–307 (2020).
- Sutter, P., Wimer, S. & Sutter, E. Chiral twisted van der Waals nanowires. *Nature* **570**, 354–357 (2019).
- Eshelby, J. D. The twist in a crystal whisker containing a dislocation. *Philos. Mag.* **3**, 440–447 (1958).
- Carruthers, P. Theory of thermal conductivity of solids at low temperatures. *Rev. Mod. Phys.* **33**, 92–138 (1961).
- Akatyeva, E. & Dumitrică, T. Eshelby twist and magic helical zinc oxide nanowires and nanotubes. *Phys. Rev. Lett.* **109**, 035501 (2012).
- Ziman, J. M. *Electrons and Phonons: The Theory of Transport Phenomena in Solids* (Oxford Univ. Press, 2001).
- Casimir, H. B. G. Note on the conduction of heat in crystals. *Physica* **5**, 495–500 (1938).
- Shi, L. et al. Measuring thermal and thermoelectric properties of one-dimensional nanostructures using a microfabricated device. *J. Heat Transf.* **125**, 881–888 (2003).
- Lee, S. et al. Anomalously low electronic thermal conductivity in metallic vanadium dioxide. *Science* **355**, 371–374 (2017).
- Ci, P. et al. Giant isotope effect of thermal conductivity in silicon nanowires. *Phys. Rev. Lett.* **128**, 085901 (2022).
- Li, W. et al. Thermal conductivity of diamond nanowires from first principles. *Phys. Rev. B* **85**, 195436 (2012).
- Bui, C. T. et al. Diameter-dependent thermal transport in individual ZnO nanowires and its correlation with surface coating and defects. *Small* **8**, 738–745 (2012).
- Guthy, C., Nam, C.-Y. & Fischer, J. E. Unusually low thermal conductivity of gallium nitride nanowires. *J. Appl. Phys.* **103**, 064319 (2008).
- Zhou, F. et al. Thermal conductivity of indium arsenide nanowires with wurtzite and zinc blende phases. *Phys. Rev. B* **83**, 205416 (2011).
- Li, D. et al. Thermal conductivity of individual silicon nanowires. *Appl. Phys. Lett.* **83**, 2934–2936 (2003).

36. Roh, J. W. et al. Size-dependent thermal conductivity of individual single-crystalline PbTe nanowires. *Appl. Phys. Lett.* **96**, 103101 (2010).
37. Li, D., Wu, Y., Fan, R., Yang, P. & Majumdar, A. Thermal conductivity of Si/SiGe superlattice nanowires. *Appl. Phys. Lett.* **83**, 3186–3188 (2003).
38. Zhang, Q. et al. Thermal transport in quasi-1D van der Waals crystal Ta₂Pd₃Se₈ nanowires: size and length dependence. *ACS Nano* **12**, 2634–2642 (2018).
39. Pan, Z., Lee, S. H., Wang, K., Mao, Z. & Li, D. Elastic stiffening induces one-dimensional phonons in thin Ta₂Se₃ nanowires. *Appl. Phys. Lett.* **120**, 062201 (2022).
40. Ly, T. H. et al. Vertically conductive MoS₂ spiral pyramid. *Adv. Mater.* **28**, 7723–7728 (2016).
41. Szot, K., Speier, W., Bihlmayer, G. & Waser, R. Switching the electrical resistance of individual dislocations in single-crystalline SrTiO₃. *Nat. Mater.* **5**, 312–320 (2006).
42. Meng, X. et al. Thermal conductivity enhancement in MoS₂ under extreme strain. *Phys. Rev. Lett.* **122**, 155901 (2019).
43. Narayan, J. & Narayan, R. Discovery of double helix and impact on nanoscale to mesoscale crystalline structures. *ACS Omega* **7**, 25853–25859 (2022).
44. Meng, F. et al. Formation of stacking faults and the screw dislocation-driven growth: a case study of aluminum nitride nanowires. *ACS Nano* **7**, 11369–11378 (2013).

Publisher's note Springer Nature remains neutral with regard to jurisdictional claims in published maps and institutional affiliations.

Springer Nature or its licensor (e.g. a society or other partner) holds exclusive rights to this article under a publishing agreement with the author(s) or other rightsholder(s); author self-archiving of the accepted manuscript version of this article is solely governed by the terms of such publishing agreement and applicable law.

© The Author(s), under exclusive licence to Springer Nature Limited 2025

Methods

Synthesis of twisted and non-twisted GeS NWs

Twisted GeS NWs and microscale crystals were synthesized using a 1 in. diameter horizontal tube furnace. The substrates used for the synthesis were (100) oriented silicon with natural oxidation. Gold catalyst material, 3 nm thick, was deposited on the substrates and patterned into bars with widths of tens of micrometres, using photolithography and electron-beam evaporation deposition. Before the synthesis, the furnace was pumped to a base pressure of 5 mtorr and flushed with argon gas blended with 4% hydrogen several times. In the synthesis, GeS powder (Sigma-Aldrich) was placed at the centre of the tube and heated to evaporate at a fixed pressure flowing with Ar/4% H₂ carrier gas, with the growth substrate placed downstream from the GeS source. The growth was performed at a pressure of 2 torr, a flow rate of 50 standard cubic centimetres per minute, a source temperature of 425 °C, a deposition temperature of 320 °C and a growth time of 20 min. The growth yields both twisted and non-twisted GeS NWs with lengths of tens to hundreds of micrometres and with varying diameters. The growth also yields twisted GeS crystals with a radial size of a few micrometres.

TEM characterization

Synthesized NWs were mechanically transferred to lacey-carbon-supported copper TEM grids for TEM analysis. TEM analysis was performed using a FEI Tecnai transmission electron microscope, operating at 200 keV. We identified both twisted and non-twisted NWs within the TEM grid. Each NW was then individually transferred using a tungsten tip manipulated with a micromanipulator to our suspended pad microdevice for thermal measurements. 4D STEM measurements of strain in twisted NWs were performed using a Thermo Fisher Spectra 200 TEM/STEM operating at 300 keV at Argonne National Laboratory. Nanodiffraction patterns were collected at every scan position using a high-speed Ceta camera with a probe-forming convergence angle of 0.5 mrad and a pixel dwell time of 200 ms. The annular dark-field STEM and the 4D STEM data sets were analysed using an open-source analysis toolkit named py4DSTEM⁴⁵ and custom-developed Python codes. The strain was calculated using the average of all measured lattice parameters as zero-strain reference. The sheared monoclinic structure of GeS was revealed by TEM analysis of a twisted GeS crystal with radial size of a few micrometres. In this analysis, a cross-sectional TEM specimen was prepared using a FEI Strata 235 dual-beam FIB system. Low-energy argon ion milling at 900 eV was further used to minimize sidewall damage and to thin the specimen for electron transparency. The sample was then imaged using the aberration-corrected TEAM 0.5 TEM in STEM mode operating at 200 keV at Lawrence Berkeley National Laboratory.

Thermal conductivity measurements

Thermal conductivities of the GeS NWs were measured using suspended pad microdevices in a vacuum chamber (<10⁻⁶ torr). The two SiN_x pads were patterned with Pt lines on top and suspended with flexible arms away from a Si substrate, as shown in the optical image in Fig. 2a. Each NW was transferred onto two suspended pads with a 5 μm gap using a sharp probe tip. Electron-beam-induced deposition was then performed in a FIB (FEI Helios G4) to bond the NW onto the underlying Pt electrodes and minimize contact thermal resistance. Electrical current was sent to the Pt microheater to heat the hot pad, and the electric resistance of the thermometers on both pads was measured via the four-probe method. By doing so, the Joule heating power (Q) in the microheater and temperature rises of the hot (ΔT_h) and cool (ΔT_c) pads were obtained, yielding $G = Q \Delta T_c / (\Delta T_h^2 - \Delta T_c^2)$. The L and d of the NWs in this study were measured using SEM to ultimately allow determination of the thermal conductivity, $\kappa = GL/\pi(d/2)^2$. We consider the potential error in the κ measurement caused by our assumption that the cross-sections of the NWs are circular. To address this, we used the

FIB to cut a few NWs in the middle and imaged their cross-sections with TEM or SEM. The results revealed a distorted polygonal cross-section of the NWs. We determine the 6% uncertainty of the measured κ due to the uncertainty of the cross-section.

Calculations (DFT)

First-principles calculations were performed on the basis of DFT using the projector augmented wave method⁴⁶ implemented in the Vienna Ab Initio Simulation Package^{47,48}. Structural optimizations and vibrational properties calculations were performed using the PBEsol exchange–correlation functional⁴⁹. All geometries were fully optimized until the forces on atoms were less than 0.005 eV Å⁻¹ (see Supplementary Note 11 for full details). Harmonic (phonon dispersions) and anharmonic (intrinsic scattering) interatomic force constants were constructed from DFT calculations on supercells with displaced atoms as implemented within phono3 and phono3py^{50,51}. The long-range Coulomb corrections to phonon frequencies were included using the dielectric constants and Born effective charges according to the method of Gonze et al.⁵². All possible interactions within the supercell are considered here. These were inputs to phono3py calculations for the bulk thermal conductivities:

$$\kappa_\alpha = \frac{1}{V} \sum_{\mathbf{q}j} C_{\mathbf{q}j} v_{\mathbf{q}j\alpha}^2 \tau_{\mathbf{q}j}$$

where V is the crystal volume, $C_{\mathbf{q}j}$ is the specific heat for the phonon mode with wavevector \mathbf{q} and polarization j , $v_{\mathbf{q}j\alpha}$ is the α component of the velocity and $\tau_{\mathbf{q}j}$ is the lifetime limited by intrinsic three-phonon scattering and phonon–isotope scattering from natural isotope mass variations⁵³. To simulate NW lattice thermal conductivity we considered cross-plane transport (z axis here corresponding to the c -axis growth direction) and included model diffuse scattering from the NW surface and ends via $1/\tau_{\mathbf{q}j}^{\text{surface}} = 2\sqrt{v_{\mathbf{q}jx}^2 + v_{\mathbf{q}jy}^2}/d$ and $1/\tau_{\mathbf{q}j}^{\text{ends}} = 2|v_{\mathbf{q}jz}|/L$, respectively, where $L = 5 \mu\text{m}$, corresponding to the gap between the thermal reservoirs of the measurement device. Calculations were done separately for orthorhombic and monoclinic GeS phases. Note that phonon–surface and phonon–isotope scattering rates are independent of temperature.

Calculations (core–shell model)

The calculated non-twisted NW κ is fully determined from the orthorhombic DFT model described above. For the twisted wires we developed a core–shell κ model (inset to Fig. 4c) to combine known features of the shell with unknown features of the core region:

$$\kappa_{\text{twist}} = \kappa_{\text{core}} \frac{r_c^2}{3r_w^2} + \kappa_{\text{shell}} \left(1 - \frac{r_c^2}{3r_w^2}\right)$$

where r_c ($0 < r_c < 30$ nm) represents the strained region near the dislocation, κ_{shell} is determined from the DFT model described above for the monoclinic structure but with $1/\tau_{\mathbf{q}j}^{\text{surface}} = 2\sqrt{v_{\mathbf{q}jx}^2 + v_{\mathbf{q}jy}^2}/(d - 2r_c)$ to account for phonons from the shell region scattering with the core region, and $\kappa_{\text{core}} = BT^{-n}$ has a weak temperature dependence ($0 < n < 1$). This model has a maximum κ value at the compressed dislocation core (κ_{core}) that decreases linearly with distance to merge smoothly with the monoclinic NW value (κ_{shell}). At lower temperatures, various extrinsic scattering mechanisms (for example, point defects, grain boundaries) can become important. Thus, we also included different types of scattering models in the fitting process to elucidate possible resistance mechanisms observed in the measured data: $1/\tau_{\mathbf{q}j}^{\text{pd}} = A\omega_{\mathbf{q}j}^4$ for point defects^{26,53} and $1/\tau_{\mathbf{q}j}^{\text{strain}} = A\omega_{\mathbf{q}j}$ for dislocation strain²⁶. Here A , B , n and r_c are fitting parameters constrained by the measured data. Our best fit is given by $A = 2.95 \times 10^{-6}$ THz³ rad⁴ (point defect), $B = 39.7$ W m⁻¹ Kⁿ⁻¹, $n = 0.25$ and $r_c = 20$ nm. See Supplementary Note 10 for detailed discussion regarding the fitting procedure and ranges of model values.

Data availability

All relevant data that support the findings are available within this article and its Supplementary Information. Optimized models for DFT calculations are available via Dryad (<https://doi.org/10.5061/dryad.rr4xgxdj6>). Source data are provided with this paper.

References

45. Savitzky, B. H. et al. Py4DSTEM: a software package for four-dimensional scanning transmission electron microscopy data analysis. *Microsc. Microanal.* **27**, 712–743 (2021).
46. Blöchl, P. E. Projector augmented-wave method. *Phys. Rev. B* **50**, 17953–17979 (1994).
47. Kresse, G. & Furthmüller, J. Efficiency of ab-initio total energy calculations for metals and semiconductors using a plane-wave basis set. *Comput. Mater. Sci.* **6**, 15–50 (1996).
48. Kresse, G. & Joubert, D. From ultrasoft pseudopotentials to the projector augmented-wave method. *Phys. Rev. B* **59**, 1758–1775 (1999).
49. Perdew, J. P. et al. Restoring the density-gradient expansion for exchange in solids and surfaces. *Phys. Rev. Lett.* **100**, 136406 (2008).
50. Togo, A. & Tanaka, I. First principles phonon calculations in materials science. *Scr. Mater.* **108**, 1–5 (2015).
51. Togo, A., Chaput, L. & Tanaka, I. Distributions of phonon lifetimes in Brillouin zones. *Phys. Rev. B* **91**, 094306 (2015).
52. Gonze, X., Charlier, J., Allan, D. C. & Teter, M. P. Interatomic force constants from first principles: the case of alpha-quartz. *Phys. Rev. B* **50**, 13035–13038 (1994).
53. Tamura, S.-I. Isotope scattering of large-wave-vector phonons in GaAs and InSb: deformation-dipole and overlap-shell models. *Phys. Rev. B* **30**, 849–854 (1984).

Acknowledgements

This work was supported by the US Department of Energy, Office of Science, Office of Basic Energy Sciences, Materials Sciences and Engineering Division, under contract DE-AC02-05CH11231 (Organic–Inorganic Nanocomposites KC3104). Thermal conductivity measurements and theoretical analysis of the strain induced structure change were supported by the US Department of Energy, Office of Science, Office of Basic Energy Sciences, Materials Sciences and Engineering Division under contract DE-AC02-05CH11231 (EMAT programme KC1201). Y.L. and Y.W. were supported by the National Science Foundation under award DMR-2340751. R.C. and J.Y. acknowledge the support from the Heising–Simons Faculty Fellowship. Y.Y. and Y.S. acknowledge support from the National Science Foundation award DMR-2145455. Work at the Molecular Foundry was supported by the Office of Science, Office of Basic

Energy Sciences, US Department of Energy, under contract DE-AC02-05CH11231. This work was performed, in part, at the Center for Nanoscale Materials, a US Department of Energy Office of Science User Facility, and supported by the US Department of Energy, Office of Science, under contract DE-AC02-06CH11357. Calculations and manuscript development (L.L.) were supported by the US Department of Energy, Office of Science, Office of Basic Energy Sciences, Material Sciences and Engineering Division. The calculations used resources of the Compute and Data Environment for Science (CADES) at the Oak Ridge National Laboratory, which is supported by the Office of Science of the US Department of Energy under contract DE-AC05-00OR22725, and resources of the National Energy Research Scientific Computing Center, which is supported by the Office of Science of the US Department of Energy under contract DE-AC02-05CH11231. We thank J. Wen at Argonne National Laboratory and N. Tamura at Lawrence Berkeley National Laboratory for assistance with the material characterization as well as Z. Fang for the NW synthesis.

Author contributions

Yin Liu, J.W. and J.Y. conceived the study. Y.W. and R.C. synthesized the GeS NW samples. L.J. performed the thermal transport measurements under the supervision of J.W. Yin Liu performed the atomic-resolution STEM imaging and Yuzi Liu, T.Z., Y.S. and Y.Y. performed the 4D STEM strain analysis. T.P., X.L., A.R. and L.L. performed the calculations and modelling of thermal conductivities. H.S. and D.C.C. simulated the structure of the metastable monoclinic structure and calculated the diffraction patterns. Yin Liu, T.P., L.L. and J.Y. wrote the manuscript with input from all the authors. All authors contributed to scientific discussion.

Competing interests

The authors declare no competing interests.

Additional information

Supplementary information The online version contains supplementary material available at <https://doi.org/10.1038/s41563-024-02108-3>.

Correspondence and requests for materials should be addressed to Yin Liu, Lucas Lindsay, Junqiao Wu or Jie Yao.

Peer review information *Nature Materials* thanks Kedar Hippalgaonkar, Jani Kotakoski and the other, anonymous, reviewer(s) for their contribution to the peer review of this work.

Reprints and permissions information is available at www.nature.com/reprints.

Anomalous thermal transport in Eshelby twisted van der Waals nanowires

In the format provided by the
authors and unedited

Table of Contents

Supplementary Note 1: Chemical analysis of twisted and non-twisted Nanowires (NWs)

Supplementary Note 2: Characterization of the NWs after e-beam induced Pt deposition

Supplementary Note 3: Electronic conductivity of NWs

Supplementary Note 4: Phonon-surface scattering

Supplementary Note 5: Scanning transmission electron microscopy (STEM) of twisted GeS crystals

Supplementary Note 6: Monoclinic GeS structure calculations

Supplementary Note 7: Strain induced monoclinic structure and selected area diffraction (SAD) patterns

Supplementary Note 8: Calculated transport properties of orthorhombic and monoclinic GeS phases

Supplementary Note 9: Temperature-dependent thermal conductivity

Supplementary Note 10: Strain maps and calculated properties with strain and compression

Supplementary Note 11: Defect-dependent thermal conductivity and core-shell model parameter fitting

Supplementary Note 12: Enhancement in κ by covalently bonded pathways

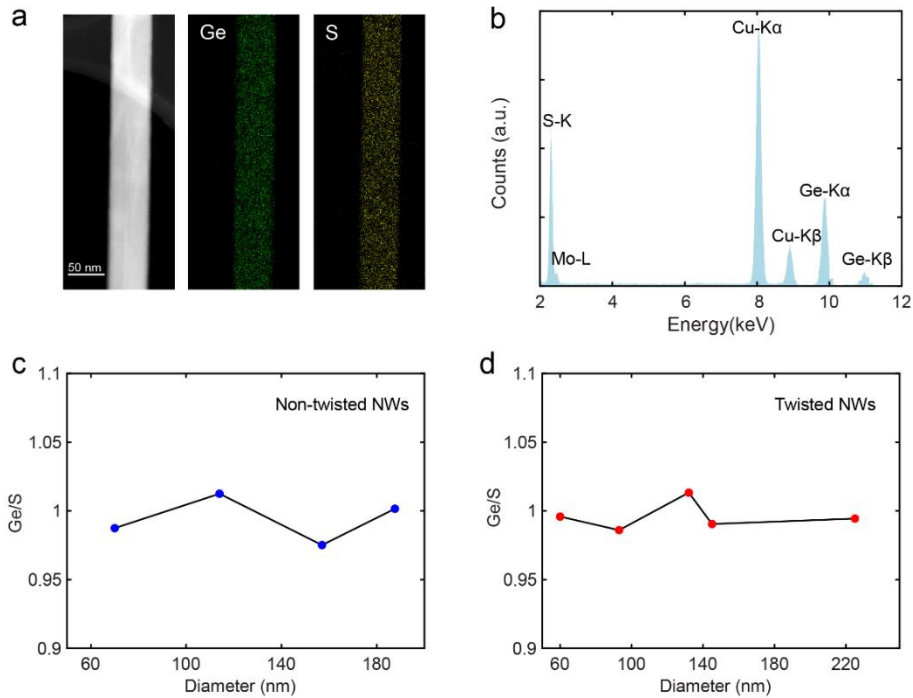
Supplementary Note 13: Extended details of density functional theory calculations

Figures S1-S19

References

Supplementary Note 1: Chemical analysis of twisted and non-twisted Nanowires (NWs)

We performed energy dispersive X-ray spectroscopy (EDS) to analyze the composition of the nanowires using a scanning transmission electron microscope (STEM). The quantitative STEM-EDS results are shown in Supplementary Fig. 1. Both twisted and non-twisted nanowires have a Ge/S ratio very close to 1:1 (the deviation is within the accuracy of the measurement, about 1 atomic percentage), exhibiting little dependence on their diameters. Based on the measured stoichiometry, it is reasonable to assume that the point defect densities are the same for nanowires with different diameters.

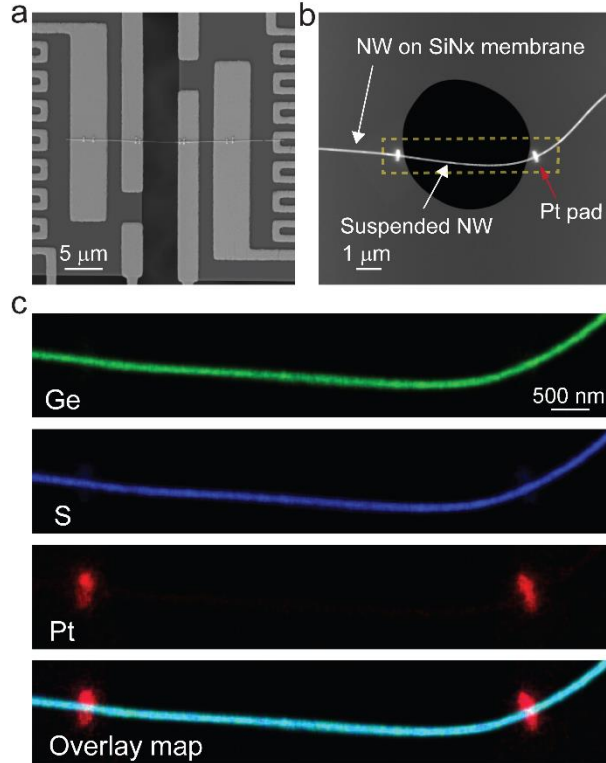


Supplementary Figure 1 **a** STEM image (left) of a selected GeS nanowire and elemental Ge and S maps (right) obtained from STEM-EDS analysis. **b** EDS spectra of the nanowire. The copper signal is from the TEM grid. **c** and **d** Atomic ratio of Ge to S for non-twisted (c) and twisted NWs (d) with varying diameters.

Supplementary Note 2: Characterization of the NWs after e-beam induced Pt deposition

Electron beam induced deposition of platinum (Pt) was subsequently carried out using a focused ion beam (FIB) system to bond the nanowire (NW) to the suspended pads, thereby minimizing contact thermal resistance. We investigate whether the electron beam-induced platinum (Pt) could potentially extend onto the suspended nanowire (NW) across the gap. This extension could result in the formation of an amorphous Pt layer on the surface of the NW, potentially impacting the measurement of thermal conductivity. We conducted TEM based chemical analysis to investigate this. We could not perform the TEM analysis on a full GeS thermal measurement device (SEM image in Supplemental Fig. 2a) due to the size mismatch between our device and the TEM sample

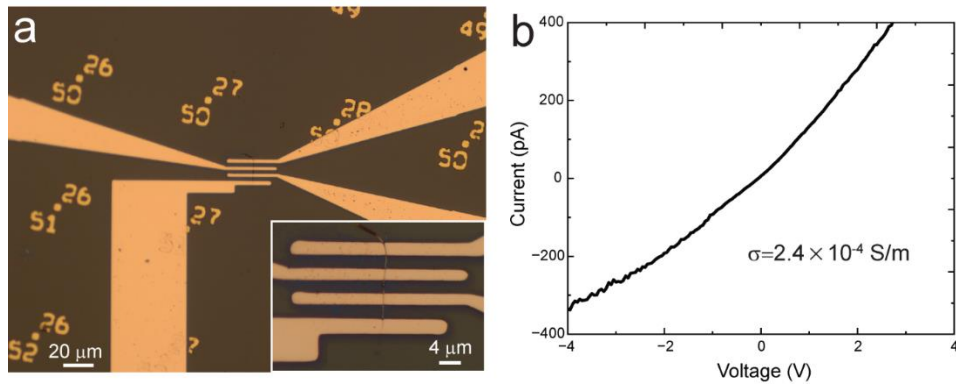
holder. Alternatively, we transferred a NW with an approximate diameter of 100 nm onto a SiN_x membrane TEM grid patterned with holes (Supplemental Fig. 2b). The SiN_x membrane is 200 nm thick, comparable to the 250 nm thickness of the SiN_x micropad. Additionally, the diameters of the holes are 5 micrometers, the same as the gap of the microdevice. We deposited Pt to bond the nanowire on the SiN_x membrane across the hole using the same deposition conditions. We then performed STEM-EDS mapping (Supplemental Fig. 2c) on the sample and detected no Pt layer in any part of the suspended region. By doing so, we ruled out the possibility of an additional Pt layer forming on our device and affecting the thermal conductivity measurements.



Supplementary Figure 2 (a) SEM image of a GeS nanowire bonded to microdevices using electron beam-induced deposition of Pt for thermal transport measurement. (b) STEM image of a nanowire transferred onto a SiN_x membrane TEM grid with patterned micro-holes. The nanowire on the TEM grid is bonded with Pt under the same deposition conditions. (c) Elemental maps of Ge, S, and Pt obtained from STEM-EDS analysis. The region mapped by EDS corresponds to the yellow dashed box in (b).

Supplementary Note 3: Electronic conductivity of NWs

We measured the electrical conductivity of twisted NWs with varying diameters on a suspended microdevice using a 2-probe method, all of which showed low electrical conductivity with no dependence on the diameter ($< 10^{-3}$ S/m). We also used a 4-probe method to measure the electrical conductivity of a twisted NW (Supplementary Fig. 3). The NW has a diameter of 130 nm, which was transferred onto a SiO_2/Si substrate for the measurement. Gold electrodes were patterned using laser direct writing lithography and electron beam evaporation. The I-V curve is approximately linear, and a conductivity of 2.4×10^{-4} S/m was extracted from the analysis. This value indicates minimal electronic contributions to the overall thermal conductivity.

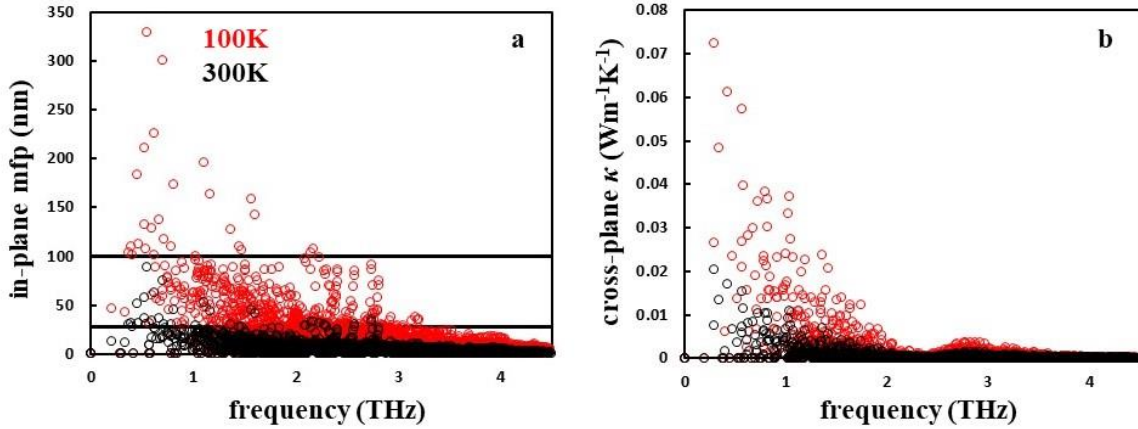


Supplementary Figure 3 **a** Optical image of a twisted NW on a SiO_2/Si substrate patterned with four gold metal probes for electrical conductivity measurements. The inset is a magnified optical image showing the NW. **b** I-V curve measured for the NW from which a conductivity of 2.4×10^{-4} S/m is extracted.

Supplementary Note 4: Phonon-surface scattering

Ultimately, transport is determined by the sum of all possible phonon modes, for which the vast majority have both in-plane and cross-plane components to their velocities. A vanishingly small subset has velocities only in- or cross-plane relative to the entire Brillouin zone. That is, most phonons contributing to transport have an in-plane component to their velocities and thus have a finite lifetime associated with diffuse scattering from the nanowire surface (see Methods of main text). Supplementary Fig. 4a shows the calculated in-plane mfps ($l_{\vec{q}jz} = |v_{\vec{q}j\alpha}| \tau_{\vec{q}j}$, where $v_{\vec{q}j\alpha}$ is the speed in the α direction for phonon mode with wavevector \vec{q} and polarization j and $\tau_{\vec{q}j}$ is the lifetime) for bulk orthorhombic GeS at $T=300$ K (black) and $T=100$ K (red) compared with $d/2$ for the largest and smallest diameter nanowires considered. Supplementary Fig. 4b shows the corresponding cross-plane mode thermal conductivities to demonstrate

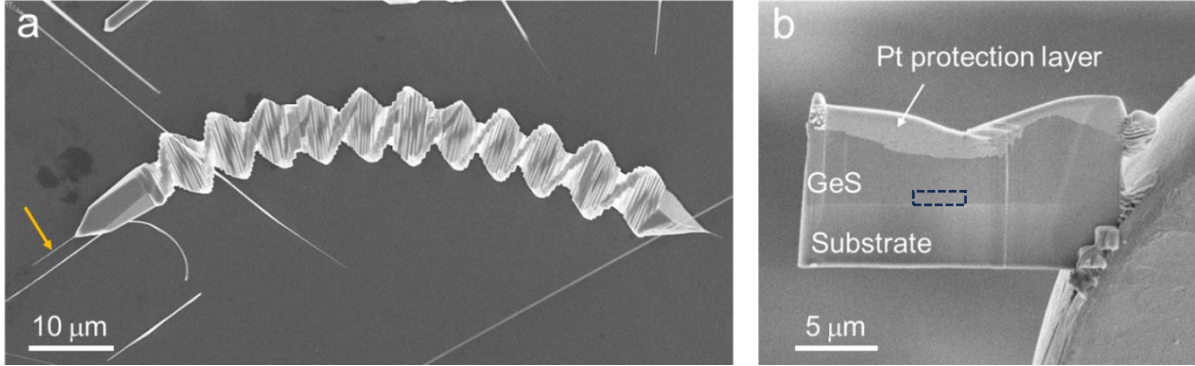
where the largest contributions occur. At T=300K, only a few modes have in-plane mfps approaching or longer than half that of the nanowire diameters considered here and thus have relatively small cross-plane κ reductions from their bulk values: 6% for the 200 nm NW and 10% for the 55 nm NW. At T=100 K, however, many modes have significantly larger in-plane mfps due to weaker anharmonic interactions and correspondingly stronger decreases in cross-plane κ : 20% for the 200 nm NW and 40% for the 55 nm NW.



Supplementary Figure 4 **a** Calculated low frequency in-plane mfps for bulk orthorhombic GeS at 300 K (black circles) and 100 K (red circles). The horizontal lines correspond to $d/2$ for the largest (top) and smallest (bottom) nanowires considered here. **b** Corresponding intrinsic mode contributions to the cross-plane κ .

Supplementary Note 5: Scanning transmission electron microscopy (STEM) of twisted GeS crystals

To investigate the dislocation-induced structural modulation in the twisted NWs, we performed analysis on a twisted GeS crystal with a radial size of a few micrometers. The growth of the twisted crystal results from radial growth of a twisted NW attached to the substrate (denoted by the arrow in Supplementary Fig. 5a). The microscale GeS crystal preserves the twist rate of the NW, thus should have a similar strain field as the twisted NWs. To prepare the sample for TEM imaging, a cross-sectional STEM specimen (Supplementary Fig. 5b) was prepared using a FEI Strata 235 dual beam focused ion beam (FIB) system. Low-energy argon ion milling at 900 eV was further used to minimize sidewall damage and to thin the specimen for electron transparency. Atomic-resolution STEM images in Fig. 3b and Fig. 3c were taken from a region close to the substrate where the initial twisted nanowire is adhered (dashed box in Supplementary Fig. 5b).



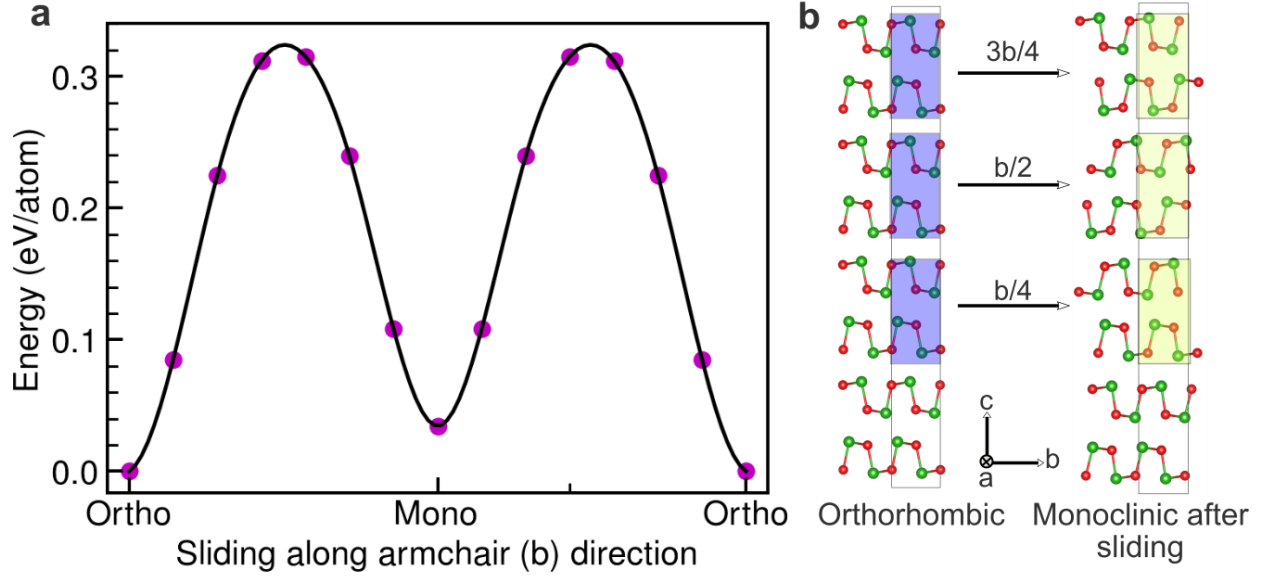
Supplementary Figure 5 **a** SEM image of a twisted GeS crystal with a diameter of a few micrometers. The yellow arrow in (a) shows the twisted NW that results in the growth of the twisted crystal. **b** SEM image of the electron transparent thin cross-sectional samples produced by FIB milling.

Supplementary Note 6: Monoclinic GeS structure calculations

The GeS monoclinic phase is constructed by following the scanning transmission electron microscopy data. The structure consists of AB stacked GeS repeated 4 times along the c -axis (4 orthorhombic GeS unit cells, 32 atoms). The first unit cell is identical to orthorhombic GeS and the second, third, and fourth unit cells are shifted by $b/4$, $b/2$, and $3b/4$, respectively, along the armchair direction (b -axis) with respect to the first unit cell. Full relaxation of the atomic positions was performed for this structure. We computed the energy barrier for the layer sliding, which gives a barrier height of ~ 0.3 eV/atom (see Supplementary Fig. 6a), indicating that such a sliding is energetically feasible. This 32-atom monoclinic structure can be represented

with an 8-atom primitive cell using the transformation matrix $\begin{bmatrix} -1 & 0 & 1/4 \\ 0 & -1 & 0 \\ 0 & 0 & 1/4 \end{bmatrix}$ identified using the spglib

library [1]. This 8-atom monoclinic cell is used in the lattice thermal conductivity calculations.



Supplementary Figure 6 **a** Calculated sliding energy for transforming the AB stacked orthorhombic (ortho) GeS phase to the monoclinic (mono) phase. Symbols are the calculated data points and the curve is a cubic spline fit. **b** Schematic showing the applied sliding mechanism.

Supplementary Note 7: Strain induced monoclinic structure and selected area diffraction (SAD) patterns

The low symmetry GeS monoclinic phase is conjectured to stem from shear stress induced by a screw dislocation and torsion in the nanowire geometry. Using isotropic elasticity theory, the displacement and strain field within a finite cylindrical nanowire containing an axial screw dislocation can be approximated with polar coordinates as [2, 3]:

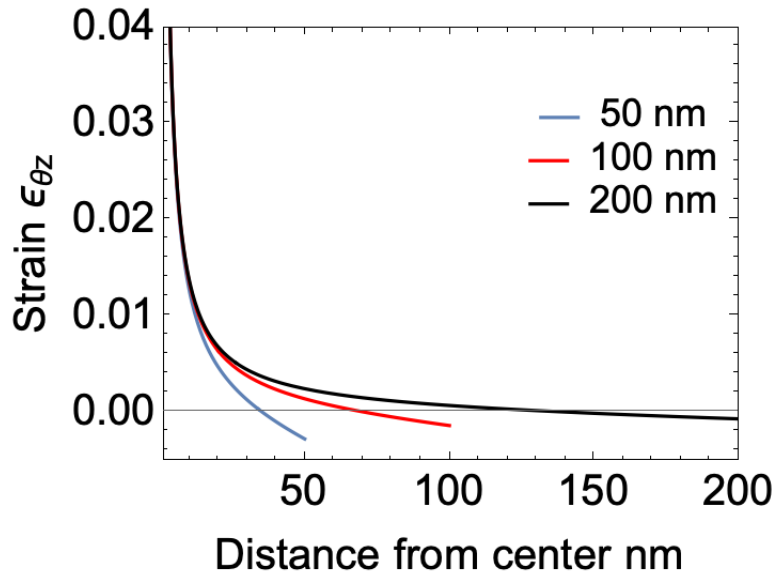
$$u_z(r, \theta) = \frac{b \theta}{2\pi}$$

$$u_\theta(r, \theta) = -\frac{b r z}{\pi R^2}$$

$$\epsilon_{\theta z}(r, \theta) = \frac{1}{2} \left(-\frac{b r}{\pi R^2} + \frac{b}{2\pi r} \right)$$

Here, u_z and u_θ represent the displacements associated with dislocation and twist, respectively. $\epsilon_{\theta z}$ denotes the resulting strain in the z -direction acting over the radial plane. R is the radius of the NW and b is the magnitude of the Burger vector.

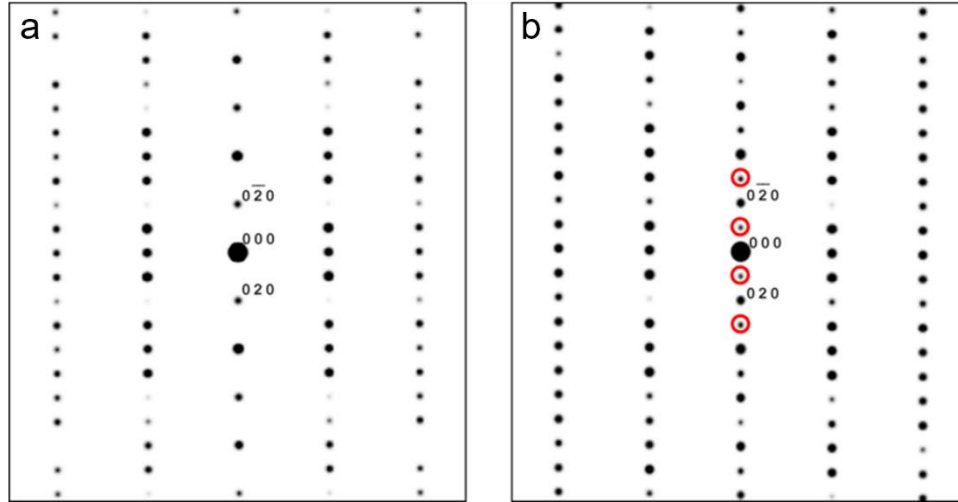
Setting $b = 1.75$ nm [4], the resulting shear strain as a function of distance from the NW center is plotted in Supplementary Fig. 7. Maximal shear stress occurs in the vicinity of the dislocation, decreasing towards the nanowire surface. The detailed elastic state of the nanowire is dependent on the size of the sample, but, in general, greater deformation is expected proximal to the core of the screw dislocation.



Supplementary Figure 7 Distribution of shear strain in twisted nanowires of different sizes.

Our STEM images of a twisted GeS nanowire reveal regions characterized by a monoclinic phase, corresponding with each double layer sliding approximately $1/4$ lattice vector along the armchair direction (b -axis). Intriguingly, this correlates with a yz shear strain (ϵ_{yz}) of about 5%, exceeding elasticity-predicted values. It seems that the low energy barrier for sliding plays an important role here. Layers can slide with respect to each other rather easily when a small amount of shear is applied. Since the shear-induced interlayer sliding can generate additional ϵ_{yz} , even a small amount of shear deformation can lead to a higher effective shear strain. To show this, we performed first principles calculations based on DFT to analyze the atomic structure of the orthorhombic cell with varying shear deformations. Before applying the deformation, the structure is fully relaxed until the maximum Hellmann-Feynman forces on each atom are below 0.01 eV/Å. The sample is then subjected to series of simple shear deformations in increments of 0.005 along the $(001)[010]$ shear direction. For each strain value, the atomic positions were relaxed within the deformed cell. It is found that interlayer sliding becomes prominent for strain values exceeding 2%.

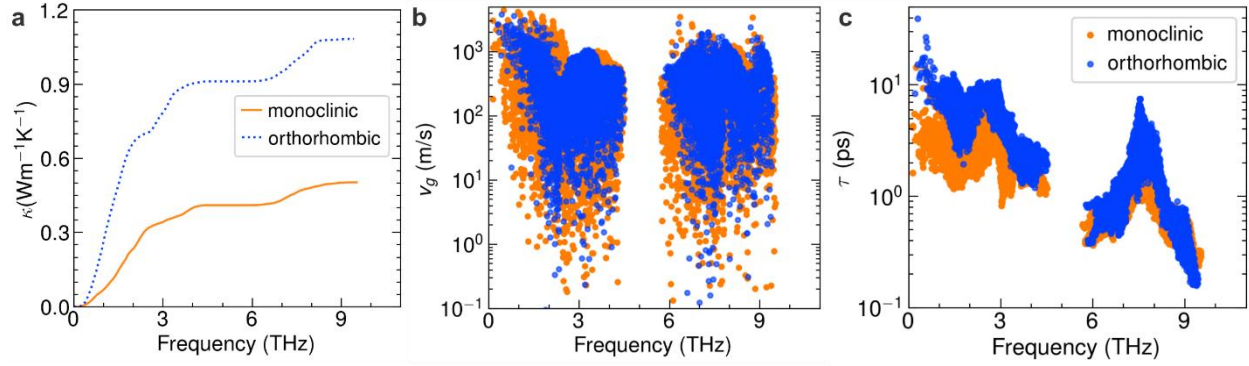
Selected area diffraction (SAD) patterns for the orthorhombic and monoclinic structures with 2.5% ϵ_{yz} were simulated with CrystalMaker software and are shown in Supplementary Fig. 8. The simulated SAD are consistent with the experimental results shown in Figs. 1 e and f of the main text. In the monoclinic structure, the glide symmetry is broken and new spots appear.



Supplementary Figure 8 Simulated electron diffraction patterns of orthorhombic (Pnma) phase (left panel) and (b) monoclinic phase (right panel) of GeS along the [110] zone axis. Red circles mark extra spots in (b) in contrast to (a).

Supplementary Note 8: Calculated transport properties of orthorhombic and monoclinic GeS phases

To identify the origin of lower lattice thermal conductivity (κ) in large twisted NWs, we present calculated cross-plane (nanowire axis) room temperature κ accumulation with frequency (Supplementary Fig. 9a), mode cross-plane group velocities (v_g ; Supplementary Fig. 9b), and mode lifetimes (τ ; Supplementary Fig. 8c) for both orthorhombic and monoclinic phases of GeS. Calculations confirm that the cross-plane κ of the monoclinic phase (twisted NWs) is significantly lower than that of the orthorhombic phase (non-twisted NWs): room temperature bulk κ values of orthorhombic and monoclinic GeS are 1.1 W/m-K and 0.52 W/m-K, respectively. Although the cross-plane group velocities are generally comparable in both phases, the room temperature phonon lifetimes are significantly lower for the monoclinic phase, as can be expected from the increased structural complexity. Thus, these smaller lifetimes are the governing factor for low thermal conductivity of the monoclinic phase.

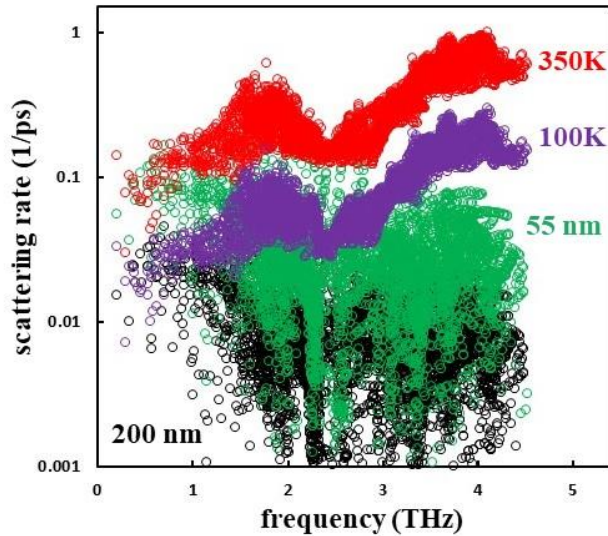


Supplementary Figure 9 a-c Comparison of (a) room temperature cross-plane accumulative lattice thermal conductivity, (b) cross-plane phonon group velocities, and (c) room temperature phonon lifetimes for orthorhombic (blue) and monoclinic (orange) phases.

Supplementary Note 9: Temperature-dependent thermal conductivity

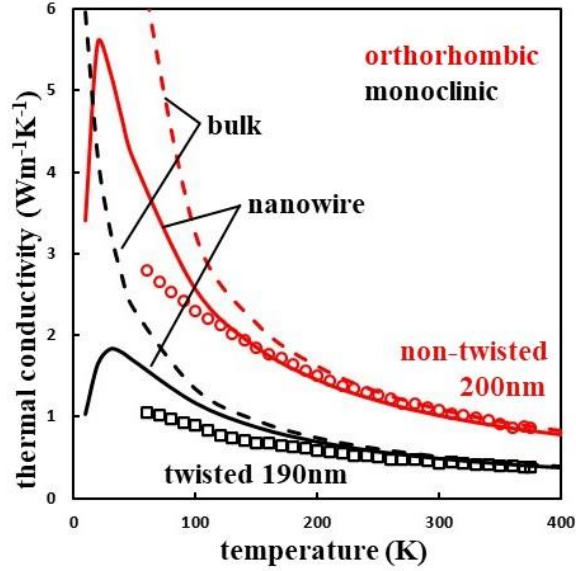
For the non-twisted GeS wires the behavior is relatively understood: at high T the intrinsic anharmonic three-phonon interactions are the dominant thermal resistance and all wires behave like bulk with $\kappa(T)$ following a $1/T$ dependence. Hence the merging of the curves near $T=350$ K. Supplementary Fig.10 compares the calculated bulk GeS orthorhombic scattering rates for three-phonon + phonon-isotope scattering rates at $T=350$ K and $T=100$ K (temperature dependent, diameter independent) with nanowire diffuse phonon-surface scattering given by $1/\tau_{\bar{q}j}^{surface} = 2\sqrt{v_{\bar{q}jx}^2 + v_{\bar{q}jy}^2}/d}$ for the $d=200$ nm and $d=55$ nm (temperature independent, diameter dependent). To determine phonon lifetimes and transport, these are combined via Matthiessen's rule $1/\tau_{\bar{q}j}^{total} = \sum_i 1/\tau_{\bar{q}j}^i$ and thus compete for dominance depending on size and temperature. For orthorhombic bulk GeS calculated κ values are 0.93 W/m-K at $T=350$ K and 3.24 W/m-K at $T=100$ K. With decreasing T the intrinsic interactions get frozen out and the T-dependence of $\kappa(T)$ weakens as the extrinsic surface scattering becomes more important, particularly for the smaller diameter NWs. Including phonon-surface scattering gives calculated thermal conductivities of: $\kappa(350$ K) $=0.88$ W/m-K and $\kappa(100$ K) $=2.61$ W/m-K for the $d=200$ nm NW and $\kappa(350$ K) $=0.79$ W/m-K and $\kappa(100$ K) $=1.95$ W/m-K for the $d=55$ nm NW. At $T=350$ K only the lowest frequency modes are affected by the surface scattering for the 55 nm wire, while at $T=100$ K surface scattering for the 200 nm NW becomes competitive at low frequency and the scattering for the 55 nm NW becomes dominant. This competition leads to the differing $\kappa(T)$ dependencies with T in going to low T. This $\kappa(T)$ dependence on diameter is similar to that observed in other nanowire systems from the literature, *e.g.*, calculations for Si nanowires for $T>100$ K [5]. However, most published data on nanowire thermal conductivity behaviors are based on covalently bonded, nearly

isotropic materials, unlike the anisotropic vdW bonded GeS NWs considered here. Measured $\kappa(T)$ for quasi-1D vdW Ta_2Se_3 [6] and $\text{Ta}_2\text{Pd}_3\text{Se}_8$ [7] nanowires also show similar temperature- and diameter-dependent behaviors compared with the non-twisted GeS wires here. However, the transport in those materials is along the covalent bonds in the chains, not along the vdW bonded directions as for the GeS NWs.



Supplementary Figure 10 Calculated bulk scattering rates for orthorhombic GeS (*no size dependence*): only intrinsic three-phonon + phonon-isotope interactions at $T=350$ K (red circles) and $T=100$ K (purple circles) compared with phonon-surface scattering rates given by $1/\tau_{\bar{q}j}^{surface} = 2\sqrt{v_{\bar{q}jx}^2 + v_{\bar{q}jy}^2}/d}$ alone (*no temperature dependence*) for $d=200$ nm (black circles) and $d=55$ nm (green circles). Note that the phonon-surface scattering rates are independent of temperature, while the bulk scattering rates are independent of nanowire size.

The $\kappa(T)$ curves of the Eshelby twisted GeS NWs and non-twisted NWs with $d>80$ nm peak at temperatures lower than measured here. The thermal conductivity peaks are dependent on the interplay of intrinsic and extrinsic scatterings; however, our calculations demonstrate that the peak $\kappa(T)$ is not very sensitive to GeS structure, variations in diameter, and reasonable model defect strengths: peak $\kappa(T)$ are ~ 20 - 30 K for the GeS NWs here (see Supplementary Fig. 11).



Supplementary Figure 11: Calculated cross-plane GeS κ for bulk (dashed curves) and nanowire geometries (solid curves) for orthorhombic (red) and monoclinic (black) structures. Measured κ data for the non-twisted 200 nm (red circles) and the twisted 190 nm NWs are shown for comparison.

Generally speaking, the higher the Debye temperature, the higher the overall κ of a material and higher in temperature the $\kappa(T)$ curve peaks. Here, we characterize the Debye temperature using [9]:

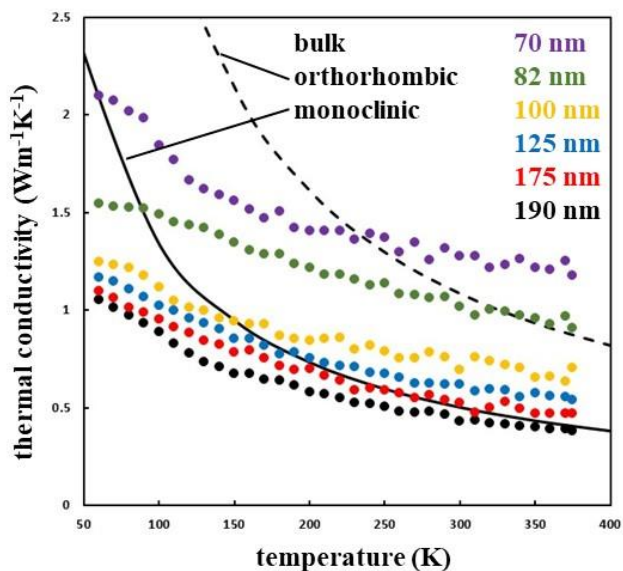
$$\theta_D = \frac{\hbar v_D}{k_B} \sqrt[3]{\frac{6\pi N}{V}}$$

where N is the number of atoms, V is the volume, and v_D is the Debye velocity which we estimate as the average low frequency transverse and longitudinal acoustic sound speeds along the c -axis. Our calculated Debye temperatures for the orthorhombic and monoclinic phases are: 336 K and 289 K, respectively. This is to be compared with calculations for other materials such as diamond (2346 K), Si (764 K), and InAs (300 K) with peak $\kappa(T)$ values at ~350 K (diamond NWs, $d \sim 100$ nm, calculated [5]), ~100-125 K (Si NWs, $d \sim 100$ nm, calculated [5] and measured [10]), and ~50 K (InAs NWs, $d \sim 100$ nm, calculated and measured [11]).

Inevitably, the measured curves should turn over with lower T and approach zero (similar to NW calculations in Supplementary Fig. 10), most likely following a T^3 power law for this range of diameters, tracking the heat capacity as is typical of materials for which boundary scattering is the dominant resistance [12, 13]. Unfortunately, we are not able to reach temperatures below 50 K given our devices and

experimental setup. Nonetheless, this behavior is well established, both theoretically [5] and experimentally [10].

For the twisted nanowires the $\kappa(T)$ behavior is confounding: (1) the $\kappa(T)$ behavior is relatively insensitive to NW diameter, (2) κ increases with decreasing diameter, and (3) κ for most of the measured data is above the intrinsic calculated monoclinic bulk values (see Supplementary Fig. 12), which again reproduce the behavior of the largest NW at the highest temperatures where intrinsic scattering is dominant. Given (3), no amount or type of extrinsic scattering in the models can alone explain the $\kappa(T)$ and diameter dependences as these would only decrease κ further.

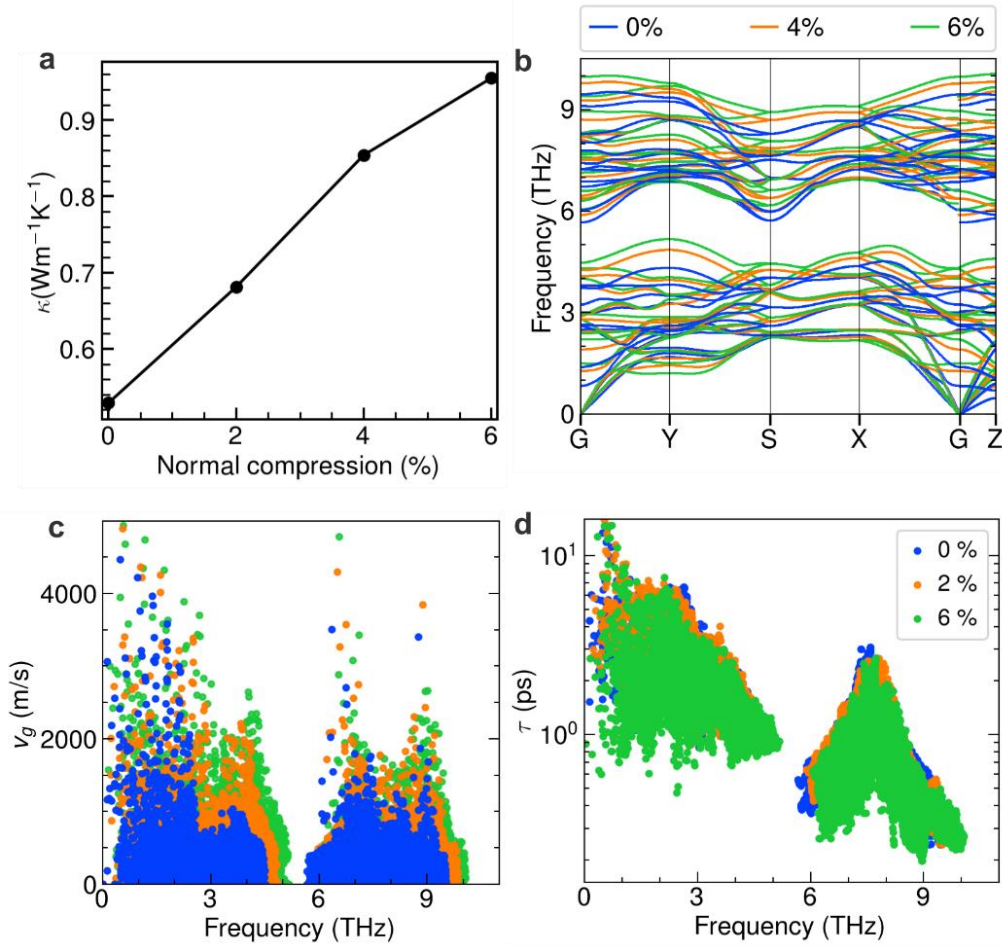


Supplementary Figure 12: Measured $\kappa(T)$ for the twisted GeS NWs compared with calculated $\kappa(T)$ for bulk monoclinic (solid curve) and orthorhombic (dashed curve) GeS.

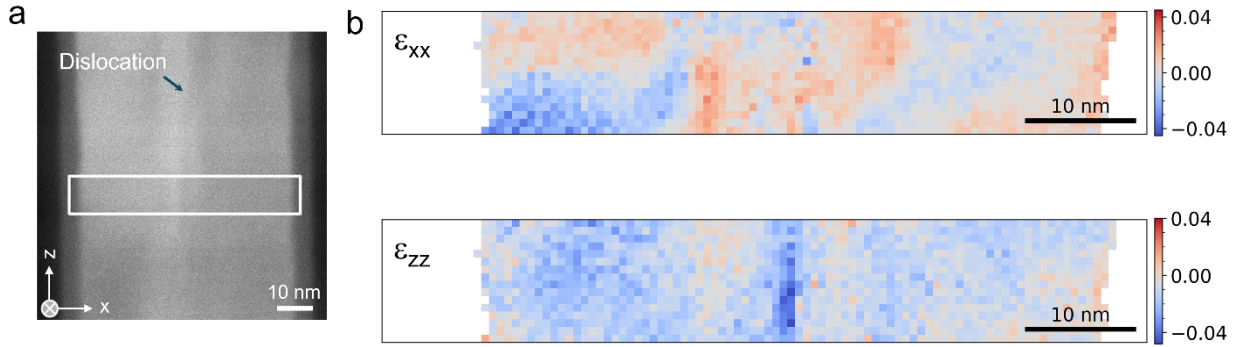
Supplementary Note 10: Strain maps and calculated properties with strain and compression

The calculated monoclinic room temperature cross-plane κ as a function of normal compression is given in Supplementary Fig. 13a. Under normal compression the κ monotonically increases from 0.52 W/m-K (unstrained) to 0.96 W/m-K (at 6% strain). To investigate the dependence of κ with normal compressive strain, we compare various vibrational properties under different strains (Supplementary Figs. 13b-d). Dispersions of both longitudinal and transverse acoustic branches are hardened with increasing strain, indicating enhancements of heat-carrier group velocities. This increase is more significant along the cross-plane direction ($G - Z$). To verify this, we plot the cross-plane component of group velocities over the entire

Brillouin zone (Supplementary Fig. 13c), which demonstrates that the cross-plane velocities are significantly enhanced under normal strain. Furthermore, strain-dependent phonon lifetimes slightly decrease with strain (Supplementary Fig. 13d). Therefore, the increase of cross-plane κ under normal compression is dominated by increasing phonon group velocities.



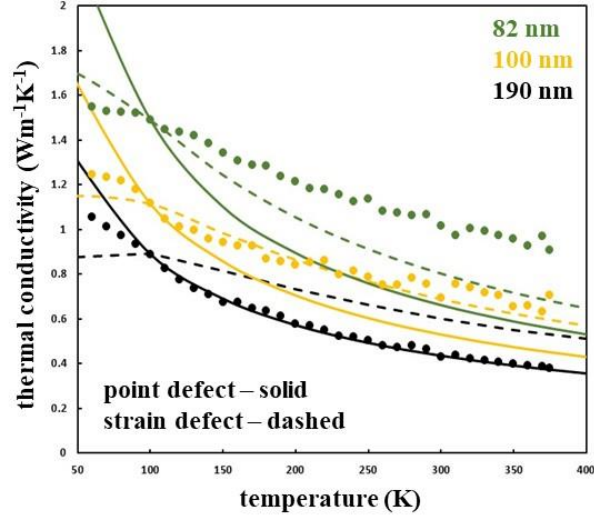
Supplementary Figure 13 a-d Calculated (a) room temperature cross-plane lattice thermal conductivity of monoclinic GeS as a function of applied normal compression. Corresponding variations of (b) phonon dispersions, (c) cross-plane group velocities, and (d) room temperature phonon lifetimes are given for selected strain values.



Supplementary Figure 14 a,b STEM image (a) and corresponding strain maps of ϵ_{xx} (upper panel) and ϵ_{zz} (lower panel) obtained from 4D STEM analysis of a twisted NW with $d=70$ nm (b). The white box in (a) denotes the area where the strain analysis is performed. The x -axis is the in-plane direction normal to (110) planes whereas the z -axis is the cross-plane direction. The electron beam is incident from the $[1\bar{1}0]$ zone axis (y -axis).

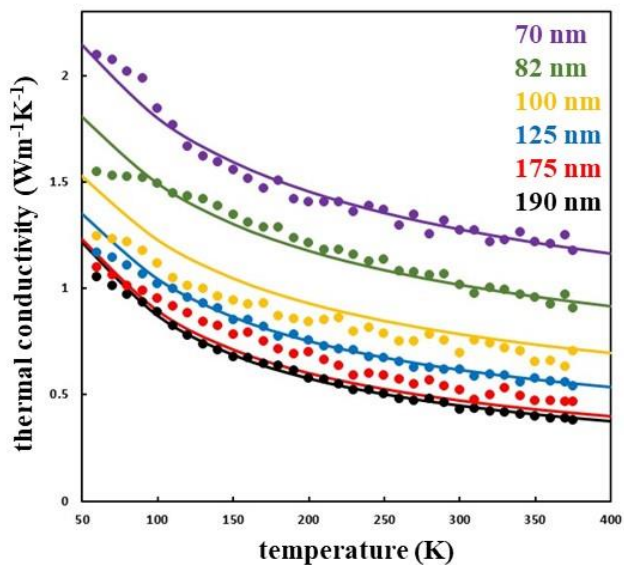
Supplementary Note 11: Defect-dependent thermal conductivity and core-shell model parameter fitting

If we presume that the GeS structure remains in the orthorhombic phase, then the proposition that the T and d behaviors are solely governed by variations in extrinsic defects with varying diameter may be possible for the nanowires with $d > 70$ nm. To test this proposition, we modeled contributions from point defect scattering ($1/\tau_{\bar{q}j}^{pd} = A\omega_{\bar{q}j}^4$ [14]) and strain dislocation scattering ($1/\tau_{\bar{q}j}^{strain} = A\omega_{\bar{q}j}$ [15]) fitting the single free parameter (A) in each case to the $T=100$ K data separately for each of the 190 nm, 100 nm, and 82 nm diameter NWs (see Supplementary Fig. 15). These fits cannot reproduce the full set of data. We note that strain fields from dislocations have been shown more significant in phonon scattering than from dislocation cores themselves [15].



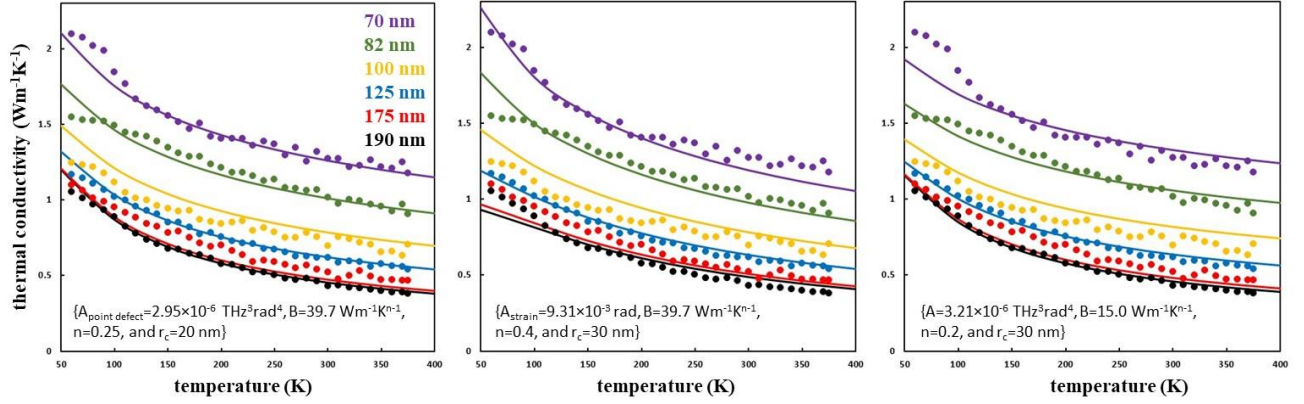
Supplementary Figure 15: Calculated $\kappa(T)$ for monoclinic GeS with intrinsic three-phonon, phonon-isotope, and nanowire boundary scattering coupled with model scattering separately from point defects (solid curves) and dislocation strain fields (dashed curves) for the 190 nm (black), 100 nm (gold), and 82 nm (green) diameter NWs compared with corresponding measurements for the twisted GeS nanowires.

We build thermal conductivity models of the twisted NWs informed by the strain measurements and DFT calculations of bulk monoclinic GeS as described in the Methods of the main manuscript. Here we provide more details of the fitting process. The only fitting parameters for the core-shell model are A , B , $0 < n < 1$, and $0 < r_c < 30 \text{ nm}$. These four parameters are constrained by the 36 $\kappa(T, d)$ data points (6 diameters at 100 K, 150 K, 200 K, 250 K, 300 K, and 350 K) for which we have both measured nanowire and calculated bulk data. Our best fit minimizing $\chi = \sum_{data} (|\kappa_{measured} - \kappa_{model}|) / \kappa_{measured}$ is shown in Supplementary Fig. 16 using $A = 2.95 \times 10^{-6} \text{ THz}^3 \text{ rad}^4$ (point defect), $B = 39.7 \text{ Wm}^{-1} \text{ K}^{-n-1}$, $n = 0.25$, and $r_c = 20 \text{ nm}$.



Supplementary Figure 16: Calculated $\kappa(T)$ (curves) compared with measured data (symbols) for the full range of twisted GeS nanowires considered here. Calculations here are from the best fit using the core-shell model described in the text with $A=2.95 \times 10^{-6} \text{ THz}^3 \text{ rad}^4$ (point defect), $B=39.7 \text{ Wm}^{-1} \text{ K}^{-n}$, $n=0.25$, and $r_c=20 \text{ nm}$.

In general, similar fits to the data can be achieved with differing core radii, but requires changing B and n to give compensating core thermal conductivities. In particular, similar fits are found using the sets: $\{B=23.6 \text{ Wm}^{-1} \text{ K}^{-n}, n=0.29, \text{ and } r_c=30 \text{ nm}\}$, $\{B=39.7 \text{ Wm}^{-1} \text{ K}^{-n}, n=0.25, \text{ and } r_c=20 \text{ nm}\}$, $\{B=235 \text{ Wm}^{-1} \text{ K}^{-n}, n=0.33, \text{ and } r_c=10 \text{ nm}\}$ which give room temperature κ values at the core of $4.56 \text{ Wm}^{-1} \text{ K}^{-1}$, $9.54 \text{ Wm}^{-1} \text{ K}^{-1}$ and $35.78 \text{ Wm}^{-1} \text{ K}^{-1}$, respectively. The larger the r_c the more reasonable the model estimates of the core thermal conductivity. We note that these variations depend very little on scattering of phonons in the shell of the material with the internal core. Removing the core term from the shell boundary scattering simply requires minor adjustments to B for similar fits. We provide examples of other fits for the core-shell model in Supplementary Fig. 17.



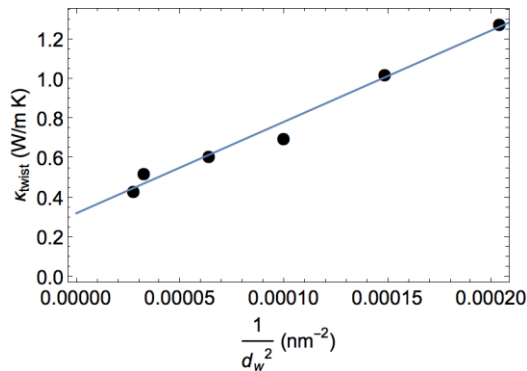
Supplementary Figure 17: Different core-shell model $\kappa(T)$ parameterizations compared with the measured twisted GeS NW κ .

Supplementary Note 12: Enhancement in κ by covalently bonded pathways

The presence of screw dislocations may introduce covalent bonds between atoms across adjacent layers, potentially creating covalently bonded paths. These bonds are primarily concentrated in the dislocation core region, which extends only a few nanometers. As a result, the region containing these covalently bonded paths is relatively small and is likely inadequate to explain the observed rise in thermal conductivity. To demonstrate this, we conducted calculations using a simple core-shell model. In this model, a cylindrical core represents the increased κ resulting from the presence of covalently bonded paths, while the shell has a lower κ without these paths. The thermal conductivity of the twisted NW is expressed as:

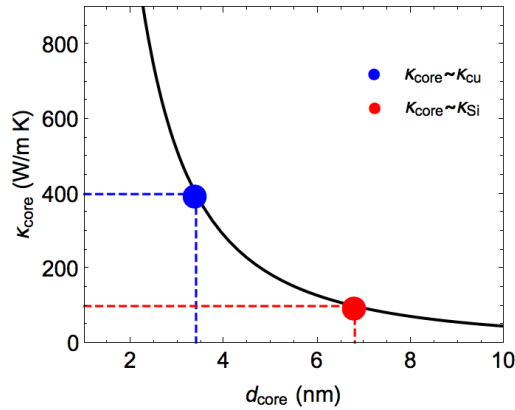
$$\kappa_{\text{twist}} = (\kappa_{\text{core}} d_c^2) \frac{1}{d_w^2} + \kappa_{\text{shell}}$$

Here, κ_{core} is the κ of the core, d_c is the diameter of the core, d_w is the diameter of the NW. We applied this model to the measured κ_{core} for different d_w values at room temperature (300K). The slope, represented as $\kappa_{\text{core}} d_c^2$, is determined as shown in Supplementary Fig. 18. The linear fitting yields a slope ($\kappa_{\text{core}} d_c^2$) of 4624.8 ($\text{W} \cdot \text{nm}^2/\text{m} \cdot \text{K}$) and an intercept of κ_{shell} of 0.323 ($\text{W} \cdot \text{m}^{-1} \cdot \text{K}$).



Supplementary Figure 18: Fit of κ_{twist} by the model

Based on the fitting, we further evaluate κ_{core} for cross-sectional size of the covalent pathway (d_{core}). Significant κ_{core} is obtained with core sizes ranging from 1 nm to 10 nm. For example, κ_{core} is as high as κ of copper if d_c is 3 nm and d_{core} is as high as κ of silicon if d_c is 7 nm. These values are significantly larger than κ of GeS (3-4 W/m K) in the covalently bonded planes (Supplementary Fig. 19). Therefore, given the spatial extension of the covalently bonded path and the values of in-plane κ of GeS, it is unlikely that this contribution is sufficient enough to lead to the observed phenomena.



Supplementary Figure 19: The thermal conductivity of the core region (κ_{core}) was evaluated for various core sizes in the core-shell model and compared with the thermal conductivities of copper (Cu) and silicon (Si)

Supplementary Note 13: Extended details of density functional theory calculations

The first-principles calculations were performed based on density functional theory (DFT) using the projector augmented wave [16] (PAW) method implemented in the Vienna ab-initio simulation package (VASP) [17, 18]. Structural optimizations and vibrational properties calculations were performed using the PBEsol exchange–correlation functional [19], a version of the PBE functional [20] revised for solids. Six ($3s^22p^4$) and fourteen ($3d^{10}4s^24p^2$) valence electrons were used in the PAW pseudo-potential for S and Ge, respectively. All geometries are fully optimized until the forces on atoms are less than $0.005 \text{ eV}\text{\AA}^{-1}$. An energy cutoff of 520 eV, energy convergence threshold of 10^{-7} eV , and a spacing of $2\pi \times 0.1 \text{\AA}^{-1}$ for k -mesh sampling in the irreducible Brillouin zone are employed for structural relaxations. The optimized lattice parameters $a = 3.66 \text{\AA}$, $b = 4.15 \text{\AA}$, and $c = 10.29 \text{\AA}$, are in reasonable agreement with the experimental values $a = 3.64 \text{\AA}$, $b = 4.29 \text{\AA}$, and $c = 10.42 \text{\AA}$ for the orthorhombic structure [21].

Calculations of lattice thermal conductivities (κ) from first principles require harmonic and anharmonic interatomic force constants (IFCs). To obtain harmonic IFCs, atoms were displaced by 0.03\AA in $4 \times 4 \times 2$

supercells using the finite displacement approach as implemented within phonopy [22]. For these displaced configurations, forces were calculated within DFT using VASP. A Γ -centered $3\times 3\times 2$ k -point mesh, energy cutoff of 520 eV, and strict energy convergence criteria of 10^{-8} eV were used to obtain converged phonon frequencies. Convergence with respect to supercell size was also verified; phonon dispersions are well converged for $4\times 4\times 2$ supercells. Anharmonic IFCs were calculated using $4\times 3\times 1$ supercells for both orthorhombic and monoclinic structures with the finite displacement scheme as implemented within phono3py [22]. All possible interactions within the supercell are considered. Here a Γ -centered $3\times 3\times 3$ k -point grid was used for Brillouin zone integrations. Other details are the same as for the harmonic IFCs. For κ calculations, the Brillouin zone was sampled on an $18\times 15\times 9$ k -mesh. In our calculations, three-phonon scattering and phonon-isotope scattering from natural isotope mass variations [23] are included.

References

1. A. Togo and I. Tanaka, Spglib: a software library for crystal symmetry search, arXiv:1808.015901.
2. J. D. Eshelby, Screw dislocations in thin rods, *J. Appl. Phys.* **24**, 176 (1953).
3. J. P. Hirth, and J. Lothe, Theory of Dislocations (Krieger, 1992).
4. Liu, Y. *et al.*, Helical van der Waals crystals with discretized Eshelby twist. *Nature* **570**, 358 (2019).
5. W. Li, N. Mingo, L. Lindsay, D. A. Broido, D. A. Stewart, and N. A. Katcho, *Phys. Rev. B* **85**, 195436 (2012).
6. Z. Pan, S. H. Lee, K. Wang, Z. Mao, and D. Li, *Appl. Phys. Lett.* **120**, 062201 (2022).
7. Q. Zhang, C. Liu, X. Liu, J. Liu, Z. Cui, Y. Zhang, L. Yang, Y. Zhao, T. T. Xu, Y. Chen, Z. Mao, and D. Li, *ACS Nano* **12**, 2634 (2018).
8. J. A. Hernandez, A. Ruiz, L. F. Fonseca, M. T. Pettes, M. Jose-Yacamán, and A. Benitez, *Sci. Rep.* **8**, 11966 (2018).
9. Ashcroft and Mermin, Solid State Physics (Thompson Learning Inc., Philadelphia, 1976).
10. D. Li, Y. Wu, P. Kim, L. Shi, P. Yang, and A. Majumdar, *Appl. Phys. Lett.* **83**, 2934 (2003).
11. F. Zhou, A. L. Moore, J. Bolinsson, A. Persson, L. Fröberg, M. T. Pettes, H. Kong, L. Rabenberg, P. Caroff, D. A. Stewart, N. Mingo, K. A. Dick, L. Samuelson, H. Linke, and L. Shi, *Phys. Rev. B* **83**, 205416 (2011).
12. H. G. B. Casimir, *Physica* **5**, 495 (1938).
13. J. M. Ziman, Electrons and Phonons (Oxford University Press, London, 1960).
14. C. A. Ratsifaritana and P. G. Klemens, *Int. J. Thermophys.* **8**, 737 (1987).
15. P. Carruthers, *Rev. Mod. Phys.* **33**, 92 (1961).
16. P. E. Blöchl, Projector augmented-wave method, *Phys. Rev. B* **50**, 17953 (1994).
17. G. Kresse & J. Furthmüller, Efficiency of ab-initio total energy calculations for metals and semiconductors using a plane-wave basis set, *Comput. Mater. Sci.* **6**, 15 (1996).
18. G. Kresse & D. Joubert, From ultrasoft pseudopotentials to the projector augmented-wave method, *Phys. Rev. B* **59**, 1758 (1999).
19. J. P. Perdew, K. Burke, & M. Ernzerhof, Generalized gradient approximation made simple, *Phys. Rev. Lett.* **77**, 3865 (1996).
20. J. P. Perdew, A. Ruzsinszky, G. I. Csonka, O. A. Vydrov, G. E. Scuseria, L. A. Constantin, X. Zhou, & K. Burke, Restoring the density-gradient expansion for exchange in solids and surfaces, *Phys. Rev. Lett.* **100**, 136406 (2008).
21. W.H. Zachariasen, The crystal lattice of germano sulphide, GeS, *Phys. Rev.* **40**, 917 (1932).

22. A. Togo, L.Chaput, T. Tadano, & I. Tanaka, Implementation strategies in phonopy and phono3py, *J. Phys. Condens. Matter* **35**, 353001 (2023).

23. S.I. Tamura, Isotope scattering of dispersive phonons in Ge, *Phys. Rev. B* **27**, 858 (1983).